


Wake bifurcations behind two circular disks in tandem arrangement

Jianzhi Yang 


Department of Built Environment, Hefei University of Technology, Hefei, Anhui 230009, China

Xiaowei Zhu

*Department of Mechanical and Materials Engineering, Portland State University,
Portland, Oregon 97207, USA*

Minghou Liu *

*Department of Thermal Science and Energy Engineering, University of Science and Technology of China,
Hefei, Anhui 230009, China*

Changjian Wang 

*Department of Built Environment, Hefei University of Technology, Hefei, Anhui 230009, China
and Anhui's International Joint Research Center of Hydrogen Safety, Hefei, Anhui 230009, China*

Yuxin Wu

School of Energy and Environment, Anhui University of Technology, Maanshan, Anhui 243002, China

Zhihe Shen

Department of Built Environment, Hefei University of Technology, Hefei, Anhui 230009, China



(Received 25 April 2021; accepted 10 June 2022; published 30 June 2022;
corrected 15 July 2022)

The wake bifurcations behind two circular disks in tandem arrangement are investigated through numerical simulations. The separation distance between the disks, S/d , is chosen at 1, 2, 4, and 6, and the Reynolds number, Re , lies in the range of $100 \leq Re \leq 500$. The wake dynamics are examined in terms of the flow structures as well as drag and lift coefficient characteristics. Seven main wake regimes are observed in the considered $(Re, S/d)$ space: steady state (SS), Zig-zig (Zz) mode, standing wave mode, periodic state with reflectional symmetry breaking (RSB), periodic state with double-helical (DH) structures shedding, periodic state with double-hairpin-loop (DHL) shedding, and weakly chaotic state. Among these bifurcations, the DH and DHL wake modes are reported in the tandem disk wakes, which are not observed in a single disk wake. Compared with the single disk wake, the first bifurcation leading to the SS mode is always delayed in tandem configuration, which is especially evident for the case of $S/d = 1$. For the second bifurcation leading to an unsteady state, some differences lie in the wake mode for different tandem configurations. The second bifurcation leads to the Zz wake mode for the cases $S/d = 1, 2$, and 4, and the RSB mode for $S/d = 6$. In the scenario of $S/d = 1$, the bifurcations are similar to those of a thick disk, suggesting that a shorter separation distance in this configuration has equivalent effects as increasing the thickness in the case of a single disk. In the scenario of $S/d = 2$, the bifurcations are complex and quite different from those in a single disk wake, indicating that the interaction between two disks in tandem arrangement is stronger when the trailing disk is located close to the end of the recirculation

*Corresponding author: mhliu@ustc.edu.cn

region of the leading one. In the scenario of $S/d = 6$, the bifurcations resemble those of a single disk wake, except for an observed DHL wake mode. In addition, the variations of the vortex shedding frequency for the unsteady states are investigated and presented.

DOI: [10.1103/PhysRevFluids.7.064102](https://doi.org/10.1103/PhysRevFluids.7.064102)

I. INTRODUCTION

The wake transition scenarios behind a three-dimensional bluff body (e.g., sphere and disk) have been extensively investigated. Researchers found that the wake behind a sphere and/or disk experiences complicated transition scenarios from steady state (SS) to chaotic state with increasing Reynolds number (see, e.g., Ern *et al.* [1]).

The investigations of wake bifurcations behind a sphere started with the global stability analysis of Natarajan and Acrivos [2], and were succeeded by the direct numerical simulation (DNS) of Ghidersa and Dusek [3], Johnson and Patel [4], Tomboulides and Orszag [5], Thompson *et al.* [6], Ormieres and Provansal [7], and Tiwari *et al.* [8]. It is noted that the detailed experiments of Ormieres and Provansal [7] yielded a consistent scenario of the first steps of the transition. The wake behind a sphere first bifurcates from a steady axisymmetric state (AS) to a steady asymmetric state at the critical Reynolds number, $Re_{c1} \approx 210$. This bifurcation leads to a SS which is a steady double-thread wake with planar symmetry. The wake first becomes unsteady with vortex shedding at the critical Reynolds number, $Re_{c2} \approx 270$, through a Hopf bifurcation. This bifurcation leads to a periodic state called the reflectional-symmetry-preserving (RSP) mode by Fabre *et al.* [9]. The wake structure in the wake mode consists of hairpin vortex loops leading the axial velocity to oscillate at the same frequency as the drag coefficient and a nonzero mean lift coefficient. The wake becomes fully three dimensional at the critical Reynolds number, $Re_{c3} \approx 420$. The vortex shedding location changes irregularly along the azimuthal direction, resulting in the breaking of planar symmetry [10].

For the wake behind a circular disk, although the first step of bifurcation is similar to that of the sphere wake, the following steps of the transition show obvious differences [9]. The wake of a circular disk is dependent on both Reynolds number and aspect ratio, which is defined as $\chi = d/w$, where d and w are the diameter and the thickness of the disk, respectively. The first bifurcation is similar to that of the sphere wake, thus leading to a SS with a planar symmetry. Natarajan and Acrivos [2] found that for the first bifurcation of a flat disk the critical Reynolds number is in the range of 115 and 117. Shenoy and Kleinstreuer [11] further reported that the second bifurcation can lead to a three-dimensional wake with hairpin vortex periodically shedding for a thin disk with aspect ratio close to 10. However, different from the sphere wake, the planar symmetry is broken in the resulting wake, leading to a reflectional-symmetry-breaking (RSB) mode. For the flat disk, the critical Reynolds number for the second bifurcation is in the range 121–125.6, and for a thin disk with aspect ratio $\chi = 10$ the critical Reynolds number is 155. Fernandes *et al.* [12] numerically investigated the first two bifurcations of the disk wake and reported that the aspect ratio is related to the critical Reynolds numbers by functions of $Re_{c1} \approx 116.5(1 + \chi^{-1})$ and $Re_{c2} \approx 125.6(1 + \chi^{-1})$. A third bifurcation leads to a periodic state with the planar symmetry recovering and the lift coefficient oscillates about a zero mean value. This wake mode is referred to as the standing wave (SW) mode by Fabre *et al.* [9] or unsteady state with planar symmetry and zero-mean lift by Shenoy and Kleinstreuer [11]. Unlike the RSP mode, the SW mode illustrates a different symmetric plane and a zero-mean lift. The critical Reynolds number is found at $Re_{c3} \approx 140$ for a flat disk, and $Re_{c3} \approx 172$ for a thin disk. Moreover, a regular shedding of hairpin vortices with planar symmetry but nonzero mean lift is then observed for the wake behind a thick disk ($\chi = 3$) by Auguste *et al.* [13] and a disk with a modest thickness ($\chi = 5$) by Yang *et al.* [14], and this wake regime is named as the Zig-zig (Zz) mode, which is similar to the RSP mode in a sphere wake. The fifth bifurcation leading to a periodic three-dimensional state with irregular rotation of the separation region is found at $Re_{c5} \approx 280$ for a thin disk ($\chi = 10$). It should be pointed out that the occurrence order of the characteristic wake regimes above is generally consistent in literature, except for a particular thick

case ($\chi = 3$). For example, the Zz wake mode is reported as the second bifurcation instead of the RSB mode for the thick disk wake [13]. Most recently, by using the numerical approach, Chrust *et al.* [15] focused on the oblate spheroids and flat cylinders in the range of $Re \in [100, 300]$ and conducted extensive parametric studies. A detailed flow regime map for a single spheroid and/or disk wake in the considered (Re, χ) space has been provided. For more information on the detailed wake bifurcations behind a single disk at low Reynolds numbers, one can refer to a recent review of Ern *et al.* [1]. As a matter of completeness, we noted the contribution from Gao *et al.* [16], who considered the flow over an inclined disk. They also observed similar wake bifurcations.

While our understanding of the wake bifurcations behind a single three-dimensional bluff body is nearly established, the bifurcations in the wake behind two adjacent bluff bodies in proximity have not been comprehensively investigated, and the physical mechanism underneath the phenomena is far from being understood. Furthermore, the wakes of multiple bodies are quite different and show higher-level complexity when compared with those of a single bluff body, which is partially because of the interactions among wakes behind the multiple bodies. As a benchmark case of multiple bodies, the flow over two three-dimensional bodies in tandem arrangement is the topic of the paper, which is widely encountered in both natural environments and engineering applications, e.g., flow around repetitive elements in structures of buildings, smoke ducts, or other civil objects [17].

The flow over two spheres positioned in tandem has been investigated by several scholars. It is reported that the wake behind two spheres in tandem is strongly dependent on the Reynolds number and the separation distance (S) between them. For $Re = 50\text{--}130$, a stagnant flow develops at $S/d = 0\text{--}2$ since the separating shear layer from the leading sphere reattaches to the trailing one [18–20]. The drag on the trailing sphere is greatly reduced compared to the case of a single sphere, while the drag of the leading one is almost unchanged. When $S/d > 2$, the reattachment disappears, and the drag on the trailing sphere increases and recovers to that on a single sphere as the separation distance increases. For $Re = 300$, three flow regimes are captured [21–24], namely, steady axisymmetric wake behind each sphere when $S/d \leq 0.7$, planar symmetric wake with vortex shedding behind each sphere when $S/d \geq 1.3$, and steady planar symmetric wake when $0.7 < S/d < 1.3$.

Compared to the sphere, the investigations on the wake behind two circular disks in tandem arrangement are even further limited. The configuration of the tandem disks has been used as flow controller [25] and non-pre-mixed flame holder [26] in combustors. By investigating the interactions between the two disks falling in tandem in a fluid at rest, with Re ranging from 80 to 300, Brosse and Ern [27,28] found that the recirculation length and drag for each disk are closely associated with the separation distance between disks. Differently, investigations on the interactions of two fixed tandem disks are usually conducted at higher Reynolds numbers. Morel and Bohn [29] studied a special case where two tandem disks have unequal diameters, and they found that the sizes of the disks and the separation distance between them have great effects on the drag reductions. Brosse and Ern [28] also performed DNS of the flow over two fixed circular disks in tandem configuration, and provided a good estimation of the motion of the objects for gaps larger than five diameters. More recently, Liu *et al.* [30] investigated the wake behind two circular disks in tandem at low to moderate Reynolds numbers: four flow regimes similar to those of a single disk wake have been identified, and the effect of the separation distance on the wake and drag experienced by each disk has been studied. However, it should be noted that the leading disk has a central hole in this paper, and the wake behind two solid circular disks (i.e., no holes) could present totally different forms.

It can be found that the wake transitions behind two three-dimensional bodies in tandem arrangement are apparently incomplete. Some questions may arise: what are the wake transition scenarios in the tandem case? Do those wake modes observed in the corresponding single bluff wake exist in the tandem case? If so, what about the critical Reynolds numbers? Are there any new wake bifurcations for the tandem configuration? How does the separation distance affect the wake transition scenarios? In order to answer these questions and fill the gap in the literature, a detailed investigation of the wake transitions behind two circular disks with equal diameters and thickness in tandem arrangement is performed in the present paper. The separation distance, S/d , is chosen at 1, 2, 4, and 6, and the Reynolds number lies in the range of $100 \leq Re \leq 500$. The flow regimes are

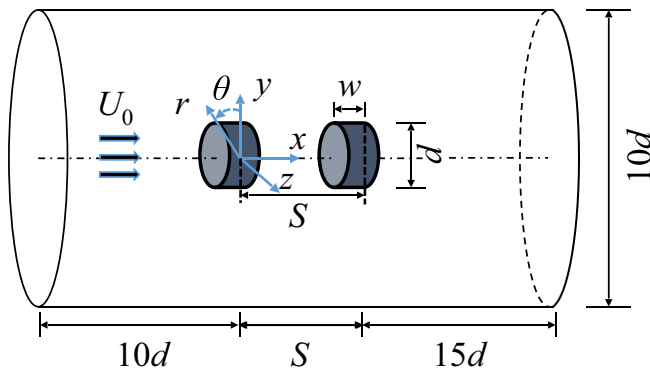


FIG. 1. The sketch of the flow configuration. Here, x , r , and θ represent the streamwise, radial, and azimuthal direction, respectively. d is the diameter of each disk, and w is the disk thickness. U_0 represents the free-stream velocity. Cartesian coordinates x , y , and z are also defined to present the results conveniently.

then identified based on the flow structures, characteristics of drag and lift coefficients, etc. We will suggest a comprehensive wake regime map for the flow over two circular disks in tandem in terms of the separation distance and Reynolds number.

The paper is organized as follows. In Sec. II, we specify the flow problem and briefly describe the numerical procedures. In Sec. III, the wake transition scenarios behind two circular disks in tandem are presented and analyzed. A comparison between the wakes behind tandem disks and a single disk is provided in Sec. IV. Finally, concluding remarks are summarized in Sec. V.

II. FLOW PROBLEM AND NUMERICAL PROCEDURE

In the present paper, large-eddy simulations (LES) of the flow over two fixed circular disks normal to the free stream in tandem arrangement, as sketched in Fig. 1, are performed. The nondimensional filtered continuity and momentum equations for incompressible flow are

$$\frac{\partial \tilde{u}_i}{\partial x_i} = 0, \quad (1)$$

$$\frac{\partial \tilde{u}_i}{\partial t} + \tilde{u}_j \frac{\partial \tilde{u}_i}{\partial x_j} = -\frac{\partial \tilde{p}}{\partial x_i} + \frac{1}{\text{Re}} \frac{\partial^2 \tilde{u}_i}{\partial x_j^2} - \frac{\partial \tau_{ij}}{\partial x_j}. \quad (2)$$

Here, $\tau_{ij} = \tilde{u}_i \tilde{u}_j - \tilde{u}_i \tilde{u}_j$ is the subgrid-scale (SGS) stress which is modeled by the dynamic Smagorinsky model [31], while $\tilde{\ast}$ indicates the spatial filtering. The Reynolds number based on the circular disk diameter, d , and the free-stream velocity, U_0 , ranges from 100 to 500. The aspect ratio $\chi = d/w = 5$, where w is the thickness of the disk, is selected, and the separation distance between the two disks, $S/d = 1, 2, 4$, and 6 , is considered. Equations (1) and (2) are, respectively, made nondimensional using d , U_0 , d/U_0 , and ρU_0^2 as characteristic length, velocity, time, and pressure.

The applied code is originally developed for simulating incompressible turbulent flows of practical relevance by LES. Owing to the high demands of LES with respect to spatial and temporal accuracies, the method is also well suited for the accurate computation of time-dependent laminar or transitional flows [32]. The code has been widely used in simulating the flow over a single disk and tandem disks [14,30,33,34]. One can refer to Yang *et al.* [14] for details and validation of the numerical code, and here only its main features are briefly recalled. The nondimensional space-filtered incompressible Navier-Stokes equations are solved on a staggered grid in a cylindrical coordinate. The diffusive terms are discretized based on a second-order central difference, the convective terms are discretized with a conservative second-order central difference [35], and the time derivatives are discretized using a second-order semi-implicit scheme. The pressure-velocity coupling is solved using the SIMPLE algorithm. It is noted that the SGS model does have little

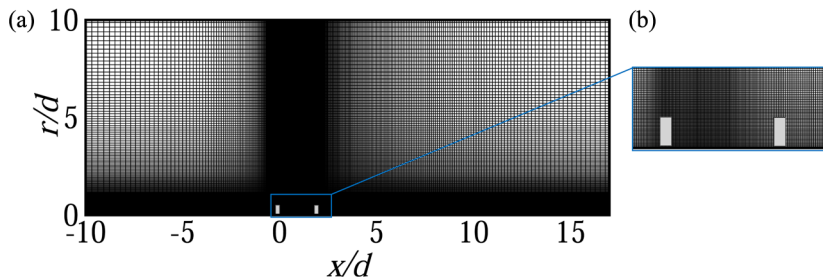


FIG. 2. (a) The view of the grid in the x - r plane for the case of $S/d = 2$ as an example. (b) The view of the grid structures near the disks.

influence, which could be estimated by the ratio of SGS viscosity to molecular viscosity, for simulating the laminar or transitional flows at the low to moderate Re considered here.

The computational domain is defined as $-10d \leq x \leq 15d + S$, $0d \leq r \leq 10d$, $0 \leq \theta \leq 2\pi$, and the leading disk is located at $10d$ from the inlet, as shown in Fig. 1. The radial and upstream extents of the computational domain are determined by considering the rate at which perturbations decay away from the disk. The origin of the coordinate system is placed at the center of the downstream surface of the leading disk with the x axis, which is the disk symmetry axis, in the free-stream direction. A Cartesian coordinate system (x, y, z) is also defined in Fig. 1 to illustrate the results more conveniently. For the boundary conditions, a nonslip boundary is imposed at the disk surface, a uniform velocity is imposed at the inflow, and a convective boundary condition is imposed ($\partial u_i / \partial t + c \partial u_i / \partial n = 0$) at the outflow and radial outer boundary. Here c is the convection velocity which is evaluated at each time step to equal the maximum outflow velocity over the outflow boundary.

The three-dimensional mesh is generated by rotating a two-dimensional Cartesian mesh about the disk axis. The mesh is refined close to the disk to properly resolve the primary features in the shear layer and near wake (see Fig. 2 for the case of $S/d = 2$ as an example). The grid resolution and domain size are determined by performing the grid independence study and domain size sensitivity analysis. For two typical conditions of $S/d = 1$ and $Re = 300$, and $S/d = 6$ and $Re = 160$, four sets of grids (see Table I) are tested for each condition. It can be found that the

TABLE I. Grid independence study control parameters, including the mesh quality, the x extent of the domain L_x/d , the grid resolution $N_x \times N_r \times N_\theta$, the amplitude of lift coefficient fluctuation A_l , recirculation length behind the trailing disk L_r/d , and the nondimensional vortex shedding frequency St .

Mesh	L_x/d	$N_x \times N_r \times N_\theta$	A_l		L_r/d	St
			Leading disk	Trailing disk		
(a) $S/d = 1$ at $Re = 300$						
Coarse	26	$128 \times 64 \times 36$	0.0252	0.0016	1.54	0.122
Standard	26	$368 \times 128 \times 72$	0.0039	0.0003	1.22	0.145
Fine	26	$440 \times 160 \times 90$	0.0036	0.0003	1.23	0.145
Fine long domain	50	$480 \times 128 \times 72$	0.0035	0.0003	1.25	0.145
(b) $S/d = 6$ at $Re = 160$						
Coarse	31	$180 \times 64 \times 36$	0.0567	0.0659	1.28	0.132
Standard	31	$480 \times 128 \times 72$	0.0337	0.0149	0.93	0.114
Fine	31	$548 \times 160 \times 90$	0.0341	0.0144	0.95	0.114
Fine long domain	50	$624 \times 128 \times 72$	0.0349	0.0138	0.97	0.114

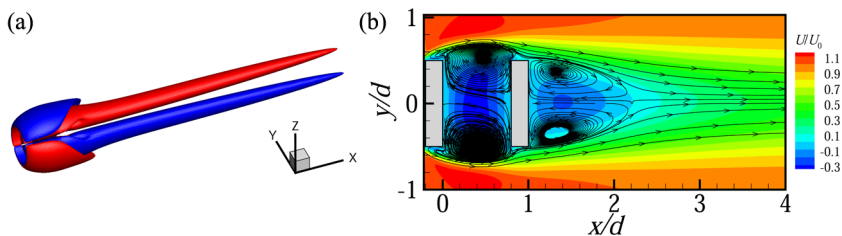


FIG. 3. The SS wake mode at $Re = 210$: (a) wake structures characterized by isosurfaces of streamwise vorticity and (b) contours of streamwise velocity in the x - y plane with in-plane streamlines.

differences in the amplitudes of lift coefficient fluctuation of each disk, recirculation length behind the trailing disk, and nondimensional vortex shedding frequency between the standard and fine grid can be negligible. Also, note that the effect of doubling the downstream length barely affects the results. Thus, the standard grid with a normal downstream length of about $15d + S$ has been selected in the present paper. The grid resolutions employed are $368(N_x) \times 128(N_r) \times 72(N_\theta)$, $400(N_x) \times 128(N_r) \times 72(N_\theta)$, $432(N_x) \times 128(N_r) \times 72(N_\theta)$, and $480(N_x) \times 128(N_r) \times 72(N_\theta)$ for the cases of $S/d = 1, 2, 4,$ and 6 , respectively. The Reynolds number is generally scrutinized with increments of $\Delta Re = 5$. However, when a new wake regime is observed, other simulations will be performed with a refined increment of $\Delta Re = 1$ in the range from the neighboring lower Re to the present Re , to determine the critical Reynolds number for each wake regime. The time step for all the cases in this paper is fixed at $0.002d/U_0$ to ensure the Courant-Friedrichs-Lewy number is less than 0.5. Typical runs consist of 65 536 time steps (corresponding to a nondimensional time tU_0/d about 131) to achieve convergence and then another 65 536 time steps will be run to output the time sequence of drag and lift coefficients, which will be used to perform the frequency spectra analysis.

III. RESULTS AND DISCUSSION

A. Bifurcations when the separation distance $S/d = 1$

When the separation distance between the two disks is short, i.e., $S/d = 1$, the bifurcations are similar to those for a single disk wake. The first bifurcation leading to a steady state with planar symmetry is captured at $Re_{c1} = 210$. Figure 3(a) shows the wake structures characterized by the isosurfaces of streamwise vorticity. A double-thread wake, i.e., a pair of steady counter-rotating streamwise vortex structures, is captured. Figure 3(b) illustrates the contours of streamwise velocity in the x - y plane with in-plane streamlines. It clearly shows that the trailing disk is located within the recirculation bubble of the leading one, resulting in squeezing of the recirculation region of the leading disk. Since the wake is the steady state with planar symmetry, the time histories of the lift components C_y and C_z of the leading and trailing disk all illustrate horizontal straight lines, as plotted in Figs. 4(a) and 4(b). In a single disk wake, this wake mode has been called the SS mode by Auguste *et al.* [13]. Even though sharing many similarities, the critical Reynolds number of $Re_{c1} = 210$ is much higher than that in a single disk wake (i.e., $Re_{c1} = 120$ in Yang *et al.* [14]), which suggests the first bifurcation is much delayed when the two disks are placed closely in tandem.

At $Re_{c2} = 285$, periodic vortex shedding occurs but the wake still remains planar symmetric, as shown in Figs. 5(a) and 5(b). Figure 5(b) depicts the wake structures characterized by the isosurface of the Q criterion [36], illustrating the periodic shedding of hairpin vortices. The lift coefficient components of both disks are oscillating about a nonzero value, as shown in Figs. 4(c) and 4(d). It is noted that the amplitudes of the lift coefficient components of both disks stay constant, and C_y and C_z for each disk vary synchronously. Therefore, the phase diagrams of the lift components of both disks illustrate straight paths located within the symmetry plane of the wake, as shown in Figs. 5(c) and 5(d). This wake mode was also observed in a single disk wake, and referred to as the unsteady

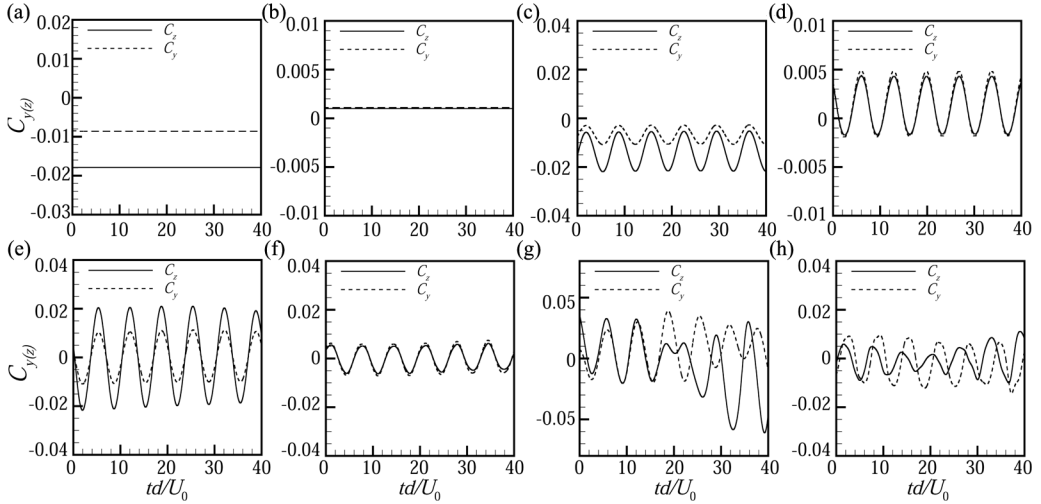


FIG. 4. The time evolutions of lift coefficients for $S/d = 1$ at (a), (b) $Re = 210$, (c), (d) $Re = 300$, (e), (f) $Re = 440$, and (g), (h) $Re = 460$. (a), (c), (e), (g) Leading disk. (b), (d), (f), (h) Trailing disk.

state with planar symmetry and nonzero mean lift by Shenoy and Kleinstreuer [11] or the Zz mode by Auguste *et al.* [13]. It is different from the usually observed second bifurcation in a single disk wake, in which a RSB mode is captured [11,14]. However, Auguste *et al.* [13] also observed the Zz mode as the second bifurcation for the wake behind a thick disk with an aspect ratio $\chi = 3$.

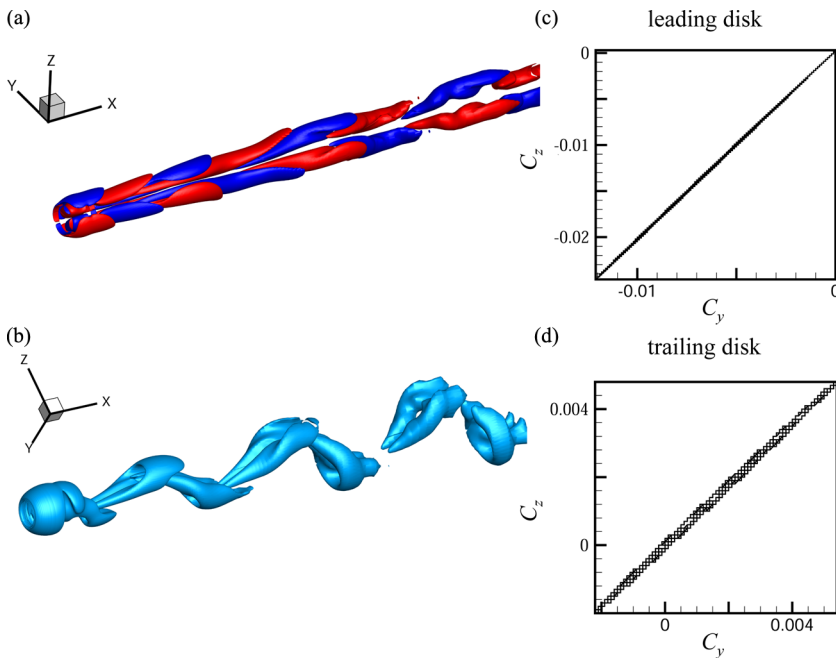


FIG. 5. The Zz wake mode at $Re = 300$ and $S/d = 1$: (a) wake structures characterized by isosurfaces of streamwise vorticity, (b) wake structures depicted by the isosurface of the Q criterion, (c) the C_y - C_z diagram of the leading disk, and (d) the C_y - C_z diagram of the trailing disk.

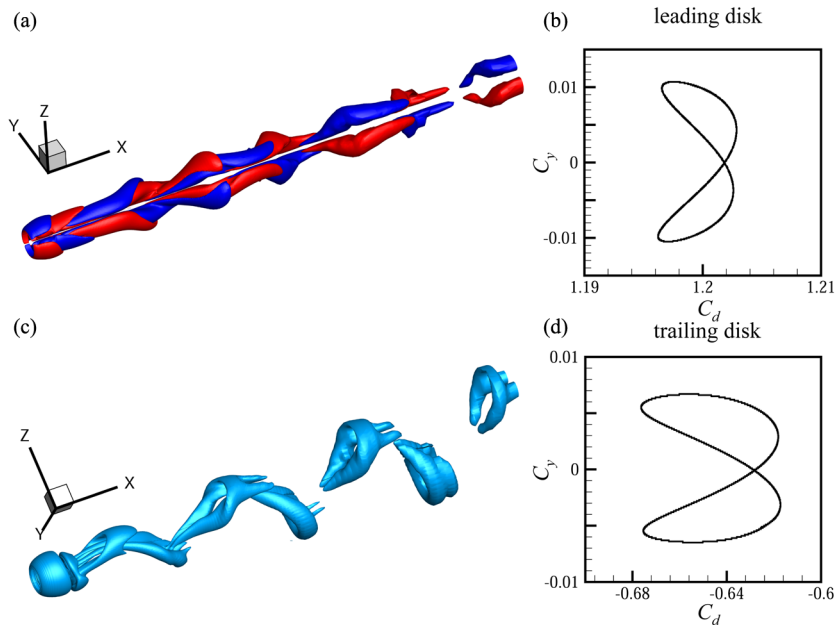


FIG. 6. The SW wake mode at $Re = 440$ and $S/d = 1$: (a) wake structures characterized by isosurfaces of streamwise vorticity, (b) wake structures depicted by the isosurface of the Q criterion, (c) the C_d - C_y diagram of the leading disk, and (d) the C_d - C_y diagram of the trailing disk.

When Re increases to $Re_{c3} = 440$, the planar symmetry of the wake is still preserved as shown in Figs. 6(a) and 6(b). However, unlike those in the Zz mode, the lift coefficient components of each disk oscillate around a mean-zero value with constant amplitudes as shown in Figs. 4(e) and 4(f). The phase diagram C_d - C_y shows a perfect butterfly shape, as shown in Figs. 6(c) and 6(d). This mode has been called the unsteady state with planar symmetry and zero-mean lift by Shenoy and Kleinstreuer [11], or the SW mode by Fabre *et al.* [9] in a single disk wake. It is worth pointing out that the occurrence order of wake modes for Zz and SW modes is opposite to that in the corresponding single disk wake (see Yang *et al.* [14]). However, the same occurrence order for the Zz and SW modes has been previously observed in the wake of a thick disk [13]. It indicates that the configuration of two circular disks placed very closely in tandem arrangement is similar to the effect of increasing the thickness of a single disk.

When Re increases further to $Re_{c4} = 460$, the wake loses its planar symmetry and becomes fully three dimensional with some small-scale structures appearing, as shown in Figs. 7(a) and 7(b). The amplitudes of the lift coefficient components of both disks are no longer constants but vary with time, as shown in Figs. 4(g) and 4(h). The phase diagrams of C_y - C_z for both disks show complex shapes, indicating the wake state is no longer regular, as shown in Figs. 7(c) and 7(d). Therefore, this wake state is referred to as the weakly chaotic (WC) state. The weakly chaotic wake mode was also witnessed by previous work on the corresponding single disk wake ($Re \geq 265$) [14].

Overall, the bifurcation scenarios in the wake behind two circular disks placed closely in tandem are similar to those in a single thick disk wake, and the only difference lies in the fact that the RSB wake mode in the single disk wake is not captured.

B. Bifurcations when the separation distance $S/d = 2$

When the separation distance increases to $S/d = 2$, the first bifurcation breaks the axisymmetry and further results in a steady state with planar symmetry, as shown in Fig. 8(a), with $Re_{c1} = 130$ in

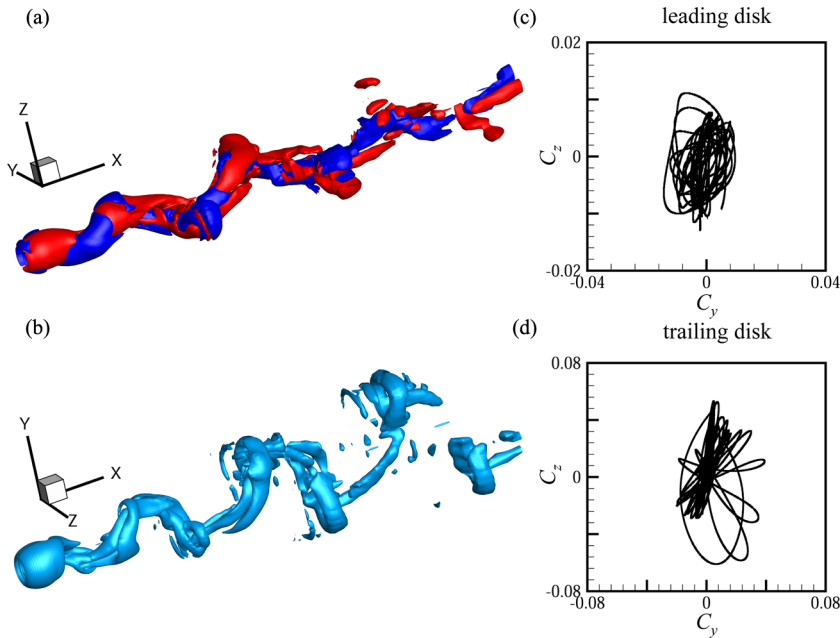


FIG. 7. The WC wake mode at $Re = 460$ and $S/d = 1$: (a) wake structures characterized by isosurfaces of streamwise vorticity, (b) wake structures depicted by the isosurface of the Q criterion, (c) the C_y - C_z diagram of the leading disk, and (d) the C_y - C_z diagram of the trailing disk.

this case. But it should be noted that this state shows some differences from the SS wake mode, e.g., the wake of the leading disk is translated to the SS mode structure while the wake of the trailing disk remains axisymmetric. This is the reason why this wake mode is referred to as the SS-AS mode. This can be further evidenced by the time histories of the lift coefficient components of each disk, as shown in Figs. 9(a) and 9(b). The lift coefficient components of the trailing disk are all zero values, indicating the axisymmetry of the wake behind the trailing disk. Figure 8(b) shows the contours of streamwise velocity in the x - y plane with in-plane streamlines, indicating that the trailing disk is located close to the end of the recirculation bubble of the leading one.

At $Re_{c2} = 140$, periodic vortex shedding occurred, while the wake remains planar symmetric. Figure 10(a) visualizes the wake structures in the form of isosurfaces of streamwise vorticity. Further inspections reveal that, even though it is very similar to Zz mode structure, the very near wake of the trailing disk is still the steady state. This can also be witnessed by the wake structure characterized by the Q criterion shown in Fig. 10(b). Here, no hairpin vortex loop has been observed in the very

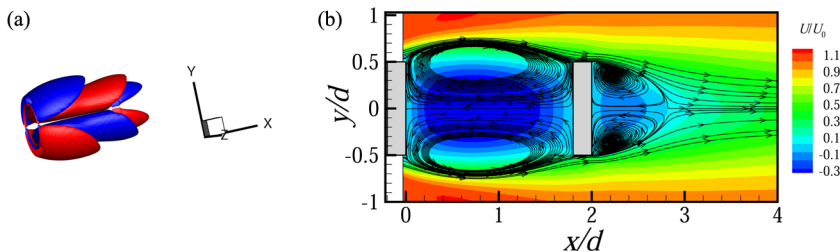


FIG. 8. The SS-AS wake mode at $Re = 130$ and $S/d = 2$: (a) wake structures characterized by isosurfaces of streamwise vorticity and (b) contours of streamwise velocity in the x - y plane with in-plane streamlines.

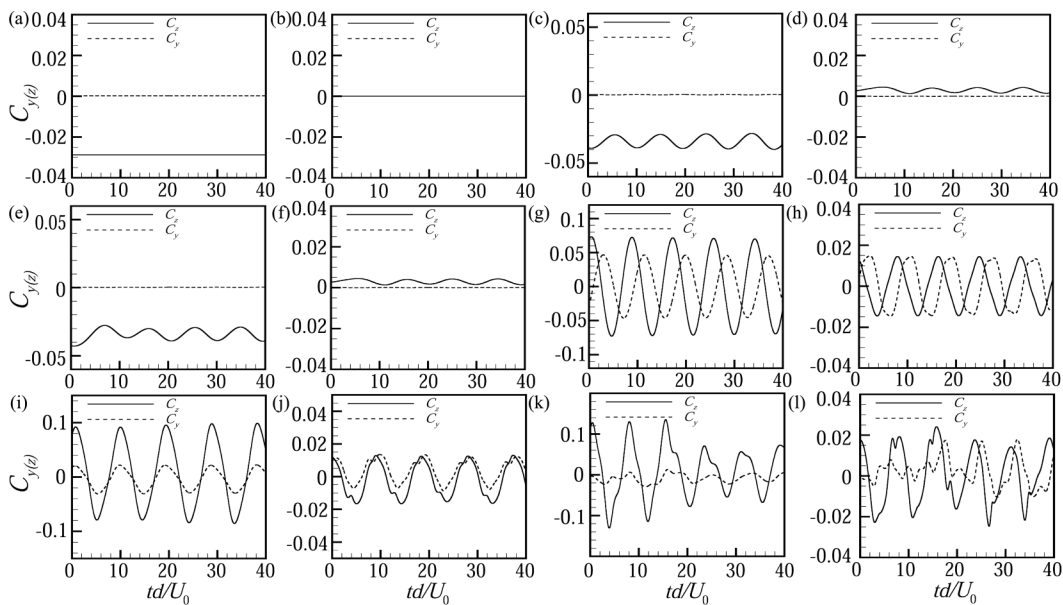


FIG. 9. The time evolutions of lift coefficients for $S/d = 2$ at (a), (b) $Re = 130$, (c), (d) $Re = 140$, (e), (f) $Re = 160$, (g), (h) $Re = 170$, (i), (j) $Re = 200$, and (k), (l) $Re = 260$. (a), (c), (e), (g), (i), (k) Leading disk. (b), (d), (f), (h), (j), (l) Trailing disk.

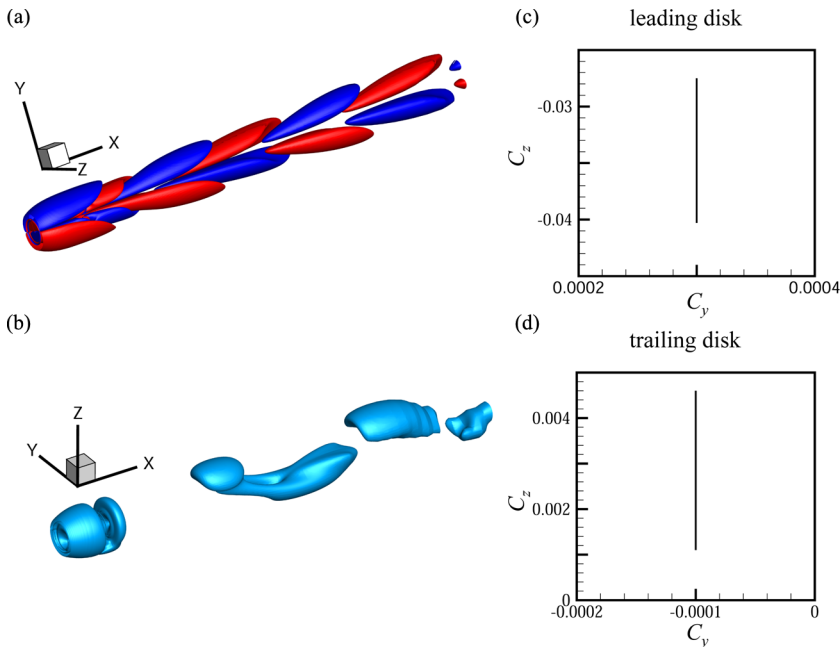


FIG. 10. The Zz -like wake mode at $Re = 140$ and $S/d = 2$: (a) wake structures characterized by isosurfaces of streamwise vorticity, (b) wake structures depicted by the isosurface of the Q criterion, (c) the C_y - C_z diagram of the leading disk, and (d) the C_y - C_z diagram of the trailing disk.

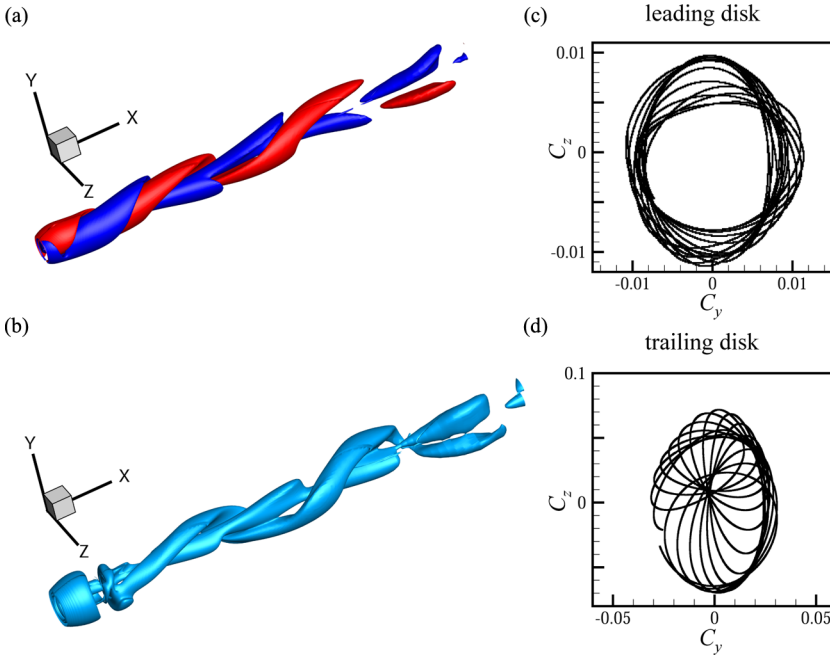


FIG. 11. The DH wake mode at $Re = 160$ and $S/d = 2$: (a) wake structures characterized by isosurfaces of streamwise vorticity, (b) wake structures depicted by the isosurface of the Q criterion, (c) the C_y - C_z diagram of the leading disk, and (d) the C_y - C_z diagram of the trailing disk.

near wake behind the trailing disk, which is because the trailing disk was placed just downstream of the recirculation region of the leading disk. Notably, the incoming flow velocity for the trailing disk is much lower than that of the leading disk. It is interesting to find that the time evolutions of the lift coefficient component C_y of both disks stay constant at very low values, as shown in Figs. 9(c) and 9(d), while the time evolutions of the lift coefficient component C_z of both disks vary periodically with constant amplitudes. The C_y - C_z diagrams of both the leading and trailing disks indicate that the lift forces are oscillating about a nonzero mean value along a vertical line within the symmetric plane, the xz plane, as shown in Figs. 10(c) and 10(d). This wake mode is referred to as the Zz -like mode to discriminate from the Zz mode. It is noted that the Zz mode is also captured at $Re_{c3} = 150$, which is observed but not shown here for brevity.

As the Reynolds number further increases to $Re_{c4} = 160$, another wake mode is detected, where an interesting double-helical (DH) structure is presented [see Figs. 11(a) and 11(b)]. The time histories of the lift coefficient components of both disks vary periodically but with amplitudes slightly changed, as shown in Figs. 9(e) and 9(f). It is noted that the phase difference between C_y and C_z of each disk also slightly changes with time. Figure 11(c) and 11(d) further show the phase diagram of lift components C_y - C_z of the leading and/or trailing disk, revealing an attractor with a complicated structure like a wool ball.

To further explore the DH wake mode, a time sequence of wake structure characterized by the isosurface of the Q criterion in one vortex shedding period is plotted in Fig. 12. At $t = t_0$, the helical structures marked with “A” and “B” begin to shed from the end of the trailing disk, as shown in Fig. 12(a). As the time proceeds, it can be seen that the azimuthal locations of the shedding of helical structures “A” and “B” rotate in an anticlockwise direction. It is notable that the radial distance of the shedding location of the helical structure marked with “A” from the trailing disk is much longer than that of the helical structure marked with “B.” Therefore, in the DH wake mode, a larger helical structure is twisted with an inner helical structure with much less amplitude.

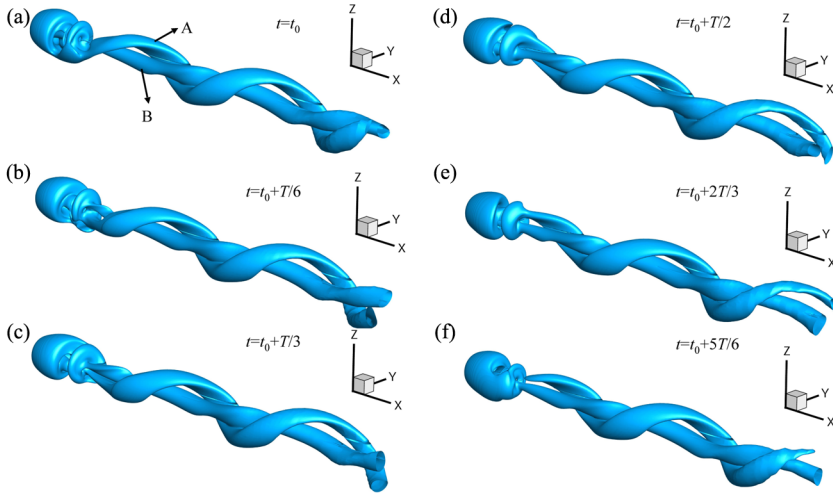


FIG. 12. A time sequence of wake structure characterized by the Q criterion for the DH wake mode at $Re = 160$ and $S/d = 2$ in one vortex-shedding period: (a) $t = t_0$, (b) $t = t_0 + T/6$, (c) $t = t_0 + 1T/3$, (d) $t = t_0 + T/2$, (e) $t = t_0 + 2T/3$, and (f) $t = t_0 + 5T/6$.

At $Re_{c5} = 170$, the double-helical structures no longer exist and a planar symmetry recovers, as shown in Figs. 13(a) and 13(b). Different from the second bifurcation mode, the lift coefficient components C_y and C_z of both disks vary periodically around a zero-mean value, as shown in Figs. 9(g) and 9(h). It is noted that the phase differences between C_y and C_z of both disks are nearly

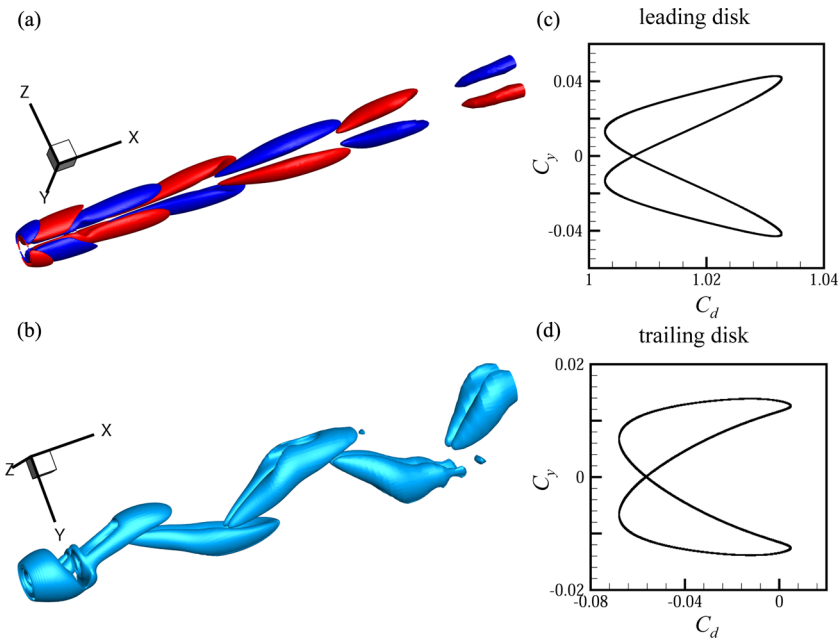


FIG. 13. The SW wake mode at $Re = 170$ and $S/d = 2$: (a) wake structures characterized by isosurfaces of streamwise vorticity, (b) wake structures depicted by the isosurface of the Q criterion, (c) the C_d - C_y diagram of the leading disk, and (d) the C_d - C_y diagram of the trailing disk.

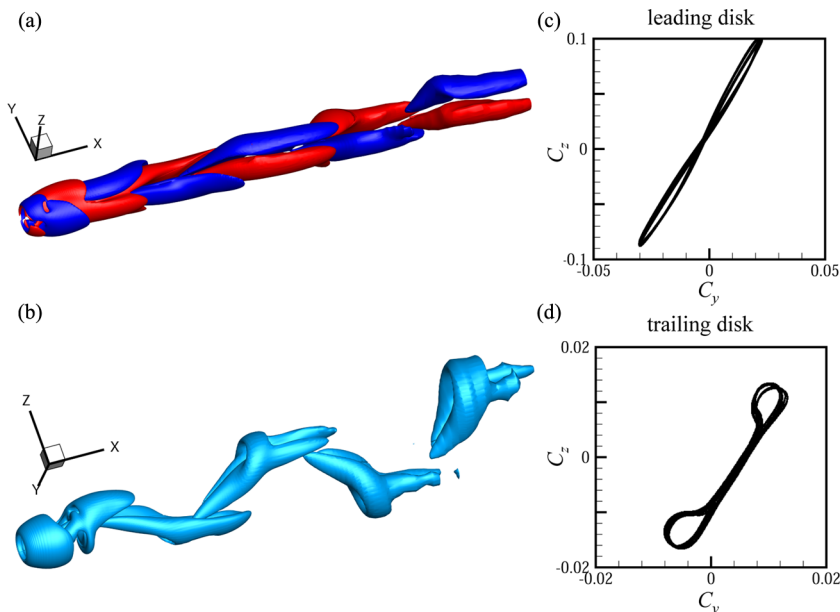


FIG. 14. The RSB-like wake mode at $Re = 200$ and $S/d = 2$: (a) wake structures characterized by isosurfaces of streamwise vorticity, (b) wake structures depicted by the isosurface of the Q criterion, (c) the C_y - C_z diagram of the leading disk, and (d) the C_y - C_z diagram of the trailing disk.

the same and vary little with time. Here, the phase diagrams of C_d - C_y for each disk are presented to illustrate a perfect butterfly shape [see Figs. 13(c) and 13(d)], which has been previously reported in the SW mode of a single disk wake [13,37], indicating that the wake now becomes the SW mode.

When the Reynolds number further increases to $Re_{c6} = 200$, the planar symmetry of the wake is broken in the very near wake behind each disk while the wake keeps “average” planar symmetry further downstream, as shown in Figs. 14(a) and 14(b). The time evolutions of the lift coefficient components C_y and C_z of each disk vary synchronously but with a very low nonzero mean value, as shown in Figs. 9(i) and 9(j). Through careful inspection, one can note that the amplitudes of the lift coefficient components change very slightly with time. Therefore, the phase diagram of the lift coefficient components C_y - C_z of the leading and/or trailing disk reveals a periodic motion with a slow pulsation superimposed, as shown in Figs. 14(a) and 14(b). This wake is referred to as the RSB-like wake mode, since the wake is mainly characterized by the breaking of planar symmetry.

When the Reynolds number increases to $Re_{c7} = 260$, the wake presents fully three-dimensional features, and a weakly chaotic state is observed. The time histories of the lift coefficient components C_y and C_z of both disks vary irregularly with amplitudes and phase differences changed with time, as shown in Figs. 9(k) and 9(l). The wake structures become fully three dimensional (not shown here for brevity).

Overall, for the configuration where the trailing disk is located close to the end of the recirculation of the leading one, the interactions between them are very strong. Meanwhile, the bifurcation scenarios become more complex and quite different from those in a single disk wake.

C. Bifurcations when the separation distance $S/d = 4$

When the separation distance increases further to $S/d = 4$, the first bifurcation is observed at $Re_{c1} = 140$. Similar to the configuration of $S/d = 2$, the wake of the leading disk breaks the axisymmetry while the wake of the trailing disk keeps the axisymmetry at the first bifurcation, as shown in Fig. 15(a). This can also be confirmed by the time evolutions of the lift coefficient

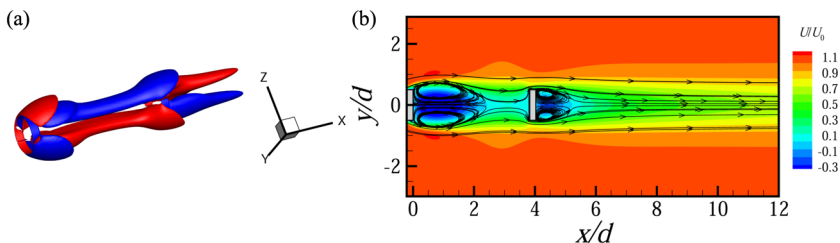


FIG. 15. The SS-AS wake mode at $Re = 140$ and $S/d = 4$: (a) wake structures characterized by isosurfaces of streamwise vorticity and (b) contours of streamwise velocity in the x - y plane with in-plane streamlines.

components C_y and C_z of the leading and trailing disk, as shown in Figs. 16(a) and 16(b). It can be found that the lift coefficient component C_y of the leading disk stays constant at a nonzero value, while both the lift components C_y and C_z for the trailing disk are at zero values. In this configuration, the trailing disk is located in the downstream of the recirculation region of the leading disk which is witnessed by Fig. 15(b), and it is noted that the momentum of the trailing disk facing is not recovered and still much lower than the free stream.

At $Re_{c2} = 145$, the second bifurcation leading to the Zz mode is captured. When the Reynolds number increases to $Re_{c3} = 160$, the Zz mode changes to the SW mode (figures for these two cases are not shown for brevity).

With Reynolds number further increased, i.e., at $Re_{c4} = 220$, a wake mode is observed. Even though the planar symmetry is still preserved with vortex shedding periodically [Fig. 17(a)], the wake structures, which can be visualized by the isosurface of the Q criterion [see Fig. 17(b)], are obviously different from those at Zz and/or SW modes. Further observation discovers a new wake mode in which each hairpin vortex structure consists of two loops in the downstream wake of the trailing disk. And thus this observed wake mode is called the double-hairpin-loop (DHL) mode. The time histories of the lift coefficient components C_y and C_z of the leading disk oscillate synchronously around a mean-zero value in perfect sinusoidal form, as shown in Fig. 16(c). However, the lift

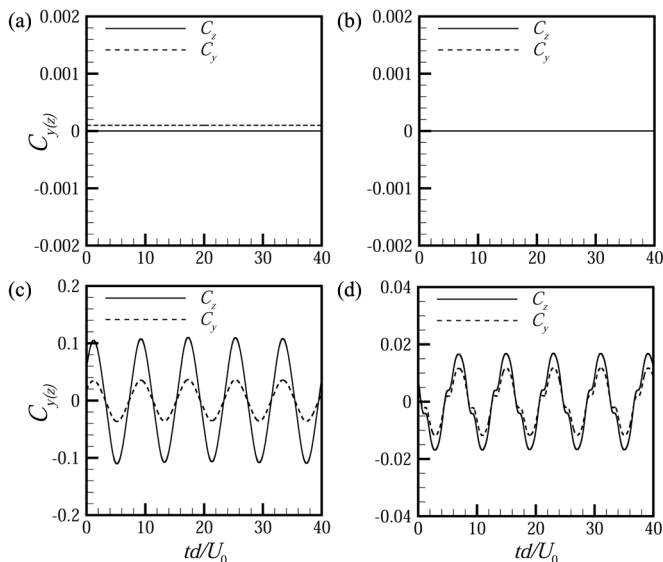


FIG. 16. The time evolutions of lift coefficients for $S/d = 4$ at (a), (b) $Re = 140$ and (c), (d) $Re = 220$. (a), (c) Leading disk. (b), (d) Trailing disk.

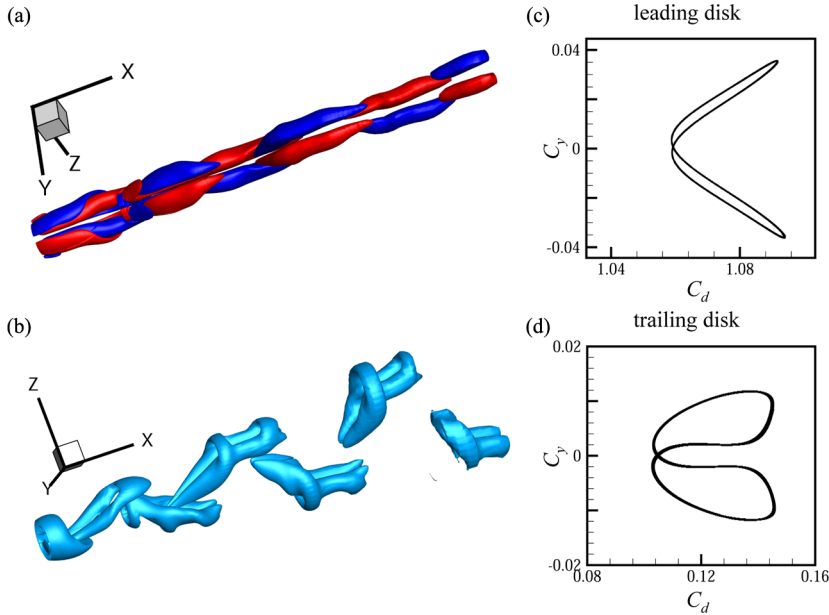


FIG. 17. The DHL wake mode at $Re = 220$ and $S/d = 4$: (a) wake structures characterized by isosurfaces of streamwise vorticity, (b) wake structures depicted by the isosurface of the Q criterion, (c) the C_d - C_y diagram of the leading disk, and (d) the C_d - C_y diagram of the trailing disk.

coefficient components C_y and C_z of the trailing disk no longer oscillate in perfect sinusoidal form due to the formation of double-hairpin loops in the wake behind the trailing disk, as shown in Fig. 16(d). It is noted that the C_y and C_z of the trailing disk also vary around a mean-zero value, indicating the planar symmetry of the wake. The phase diagrams of C_d - C_y of both leading and trailing disks illustrate butterflylike shapes, indicating the drag coefficient varies twice as much as the lift coefficient in one period, as shown in Figs. 17(c) and 17(d).

To explore the physical mechanisms of the DHL wake mode, a time sequence of wake structures characterized by the isosurface of the Q criterion in a vortex shedding period is depicted in Fig. 18. At $t = t_0$, a single vortex loop marked with “A” shedding from the leading disk reaches the trailing disk, as shown in Fig. 18(a). Then, this vortex loop interacts with the shear layer developed from the trailing disk as shown in Fig. 18(b). Meanwhile, a vortex loop marked with “B” shedding from the trailing disk begins to form at $t = t_0 + T/3$ as shown in Fig. 18(c). While the time further proceeds, the hairpin loops “A” and “B” interact with each other and are further convected downstream, as shown in Figs. 18(d) and 18(e). Finally, a double-hairpin-loop structure is formed, and it is noted that another new hairpin loop shedding from the leading disk is convected to reach the trailing disk, as shown in Fig. 18(f). Therefore, the DHL wake structure is generated due to the strong interaction of the hairpin loops shedding from the leading and trailing disks. It should be recalled that the double-hairpin loops are shedding from diametrically opposite orientations, and the description of the generation of only one double-hairpin loop is given here. The WC mode occurs when the Reynolds number increases to $Re_{c5} = 300$ (also not shown for brevity).

D. Bifurcations when the separation distance $S/d = 6$

For the configuration of two disks in tandem with separation distance $S/d = 6$, the interactions between the wakes of the leading and trailing disks are expected to be weaker. At $Re_{c1} = 140$, both wakes behind the leading and trailing disks are changed to the SS mode, as shown in Fig. 19(a). For this configuration, as the trailing disk is located at the downstream wake of the leading one,

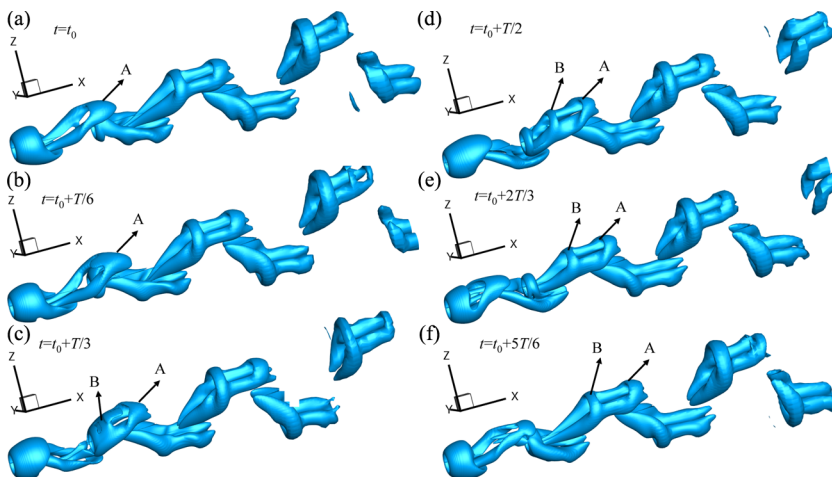


FIG. 18. A time sequence of wake structure characterized by the Q criterion for the DHL wake mode at $Re = 220$ and $S/d = 4$ in one vortex-shedding period: (a) $t = t_0$, (b) $t = t_0 + T/6$, (c) $t = t_0 + T/3$, (d) $t = t_0 + T/2$, (e) $t = t_0 + 2T/3$, and (f) $t = t_0 + 5T/6$.

the momentum of the trailing disk facing is still less than the incoming free-stream flow (i.e., the momentum of the leading disk facing), even though the momentum has been partially recovered, as shown in Fig. 19(b). As expected, the time evolutions of the lift coefficient components of both disks illustrate constant lines, and the values of C_y of both disks are nonzero, as shown in Figs. 20(a) and 20(b). To distinguish the difference from the SS mode for a single disk wake, this mode is referred to as the SS-SS mode. The predicted critical Reynolds number $Re_{c1} = 140$ is a little higher than that for a single disk wake (i.e., $Re_{c1} = 120$ in Yang *et al.* [14]).

At $Re_{c2} = 146$, a Hopf bifurcation leading to breaking of the planar symmetry with vortex shedding periodically is captured. The wake structures of both leading and trailing disks are very similar to the RSB mode detected in a single disk wake, as shown in Figs. 21(a) and 21(b). The time evolutions of the lift coefficient components C_y and C_z of each disk vary periodically with a low nonzero mean value, as shown in Figs. 20(c) and 20(d). Similar to the RSB mode captured for $Re = 200$ and $S/d = 2$, one can note that the amplitudes of the lift coefficient components change very slightly with time through careful inspection. This can also be seen from the phase diagrams of the C_y - C_z of both disks shown in Figs. 21(c) and 21(d), which illustrate nonclosed loops. In a similar manner, we call this wake regime the RSB-RSB mode to be distinguished from the single disk case.

When Reynolds number increases to $Re_{c3} = 160$, the planar symmetry recovers for wake structures behind both the leading and trailing disks, as shown in Figs. 22(a) and 22(b). Similar to the SW mode for $S/d = 2$ shown in Figs. 9(g) and 9(h), the time histories of the lift coefficient components

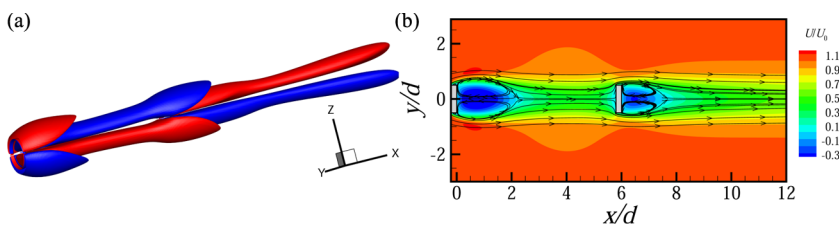


FIG. 19. The SS-SS wake mode at $Re = 140$ and $S/d = 6$: (a) wake structures characterized by isosurfaces of streamwise vorticity and (b) contours of streamwise velocity in the x - y plane with in-plane streamlines.

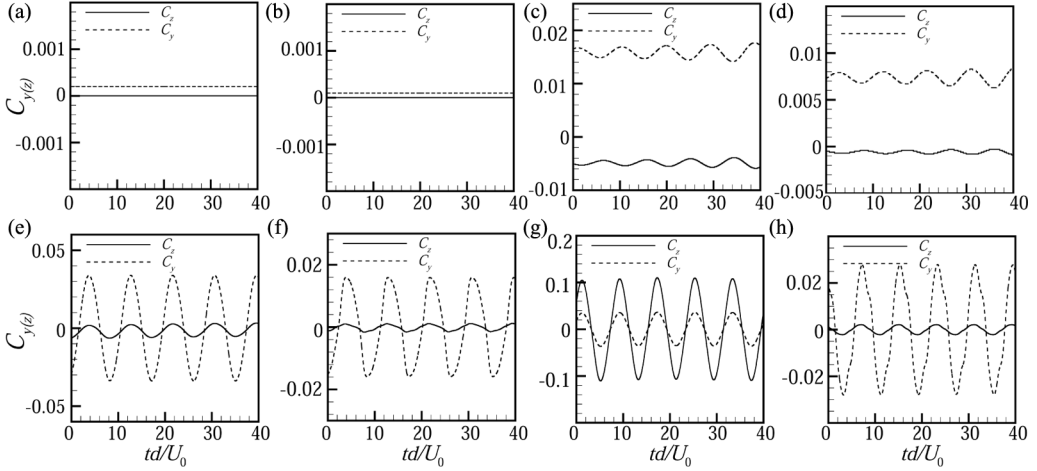


FIG. 20. The time evolutions of lift coefficients for $S/d = 6$ at (a), (b) $Re = 140$, (c), (d) $Re = 150$, (e), (f) $Re = 160$, and (g), (h) $Re = 220$. (a), (c), (e), (g) Leading disk. (b), (d), (f), (h) Trailing disk.

C_y and C_z of both disks vary periodically around zero-mean values with constant amplitudes as shown in Figs. 20(e) and 20(f). And the phase diagrams of the drag-lift components C_d - C_y of both leading and trailing disk illustrate butterfly shapes, as shown in Figs. 22(c) and 22(d). Therefore, this mode is referred to as the SW-SW mode to be distinguished from the SW mode in a single disk wake.

The fourth bifurcation observed in the case of $S/d = 4$, i.e., the DHL wake mode, is also captured when the Reynolds number increases to $Re_{c4} = 220$. Similar to the DHL mode shown in Figs. 16(c)

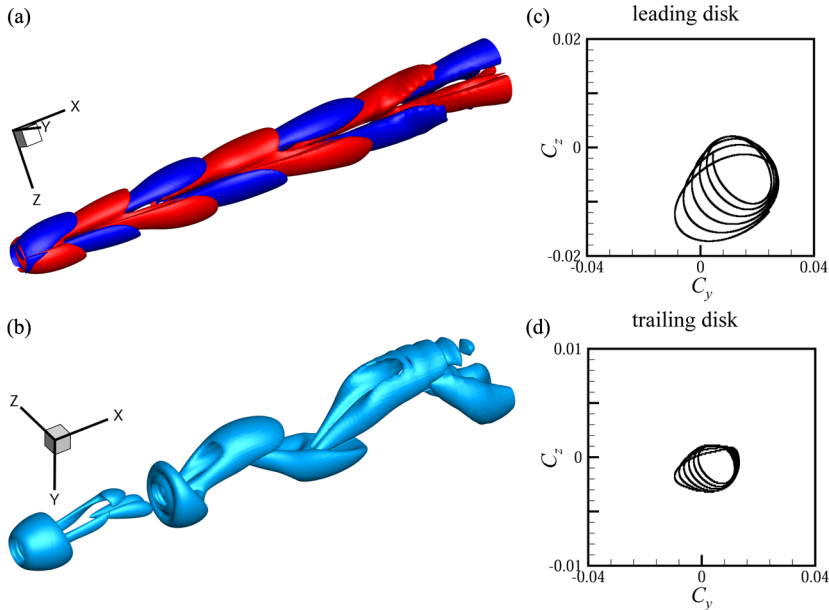


FIG. 21. The RSB-RSB wake mode at $Re = 150$ and $S/d = 6$: (a) wake structures characterized by isosurfaces of streamwise vorticity, (b) wake structures depicted by the isosurface of the Q criterion, (c) the C_y - C_z diagram of the leading disk, and (d) the C_y - C_z diagram of the trailing disk.

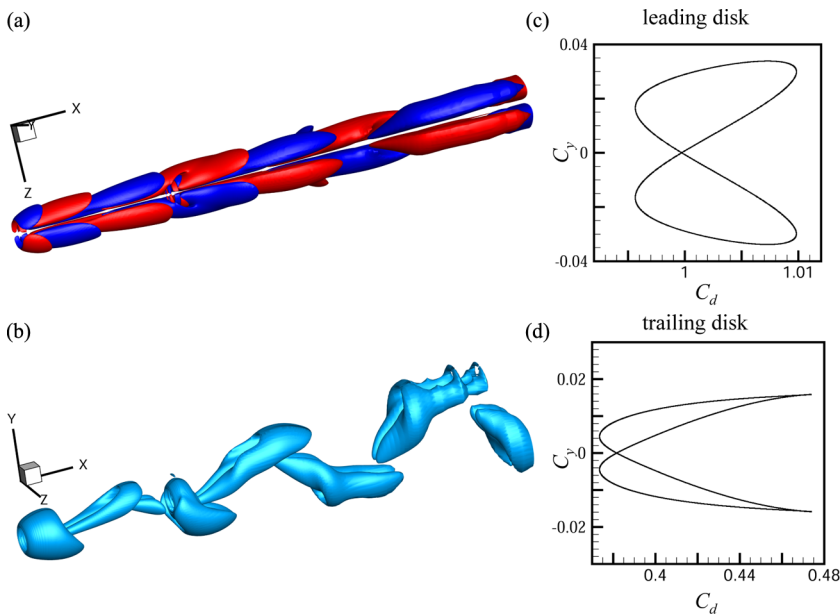


FIG. 22. The SW-SW wake mode at $Re = 160$ and $S/d = 6$: (a) wake structures characterized by isosurfaces of streamwise vorticity, (b) wake structures depicted by the isosurface of the Q criterion, (c) the C_d - C_y diagram of the leading disk, and (d) the C_d - C_y diagram of the trailing disk.

and 16(d), the time histories of the lift coefficient components of both disks vary around mean-zero values, but the lift coefficient components of the trailing disk no longer vary in perfect sinusoidal forms, as shown in Figs. 20(g) and 20(h). The wake structures are not shown here for brevity. When the Reynolds number further increases to $Re_{c5} = 300$, the wake becomes fully three dimensional and changes to the WC mode.

Overall, for the configuration of two disks in tandem arrangement with a large separation distance, the wake bifurcations behind each disk are very similar to those in a single disk due to the weak interactions between the wakes of the leading and trailing disks. But it should be pointed out that even in the case of $S/d = 6$ the interactions between the wakes behind the leading and trailing disks do not vanish.

E. Frequency analysis

In this subsection, we further examine the wake regimes and bifurcations in terms of frequency components from spectra obtained by computing the fast Fourier transform of the time histories of the drag and lift coefficients of each disk. Note that the same logarithmic scale is used for all frequency spectra aiming at establishing a quantitative comparison.

For the separation distance of $S/d = 1$, there are only three unsteady states observed. For the Zz mode at $Re = 300$, the frequency spectra of the lift coefficients of the leading and trailing disks illustrate dominant peaks at $St = fd/U_0 = 0.145$ (where St is the Strouhal number and f is the frequency) and the spectra of drag coefficients of both disks also illustrate dominant peaks at the second harmonics, i.e., $2St$, as shown in Figs. 23(a) and 23(b). This characteristic frequency is associated with the vortex shedding of hairpin vortex structures. As shown in Figs. 23(c) and 23(d), for the SW mode at $Re = 440$, the frequency spectra of the lift coefficients for both disks also illustrate dominant peaks at about $St = 0.145$, while the spectra of the drag coefficient of both disks capture dominant peaks at about $2St$, which is consistent with the phase diagram of C_d - C_y , i.e., the C_d varies two times in one period of C_y , as shown in Figs. 6(c) and 6(d). When

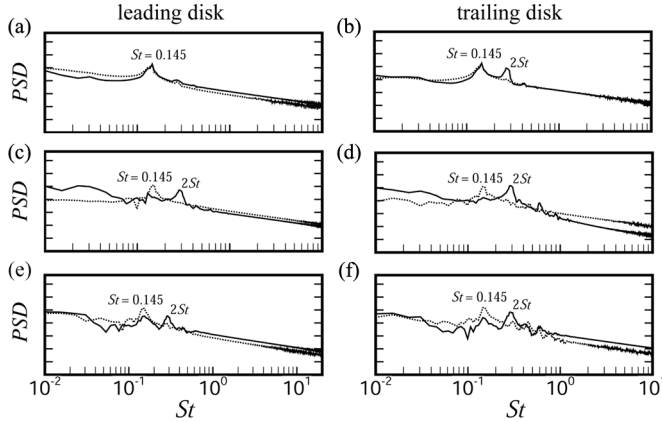


FIG. 23. Frequency spectra of drag and lift coefficients for $S/d = 1$ at (a), (b) $Re = 300$, (c), (d) $Re = 440$, and (e), (f) $Re = 460$. (a), (c), (e) Leading disk. (b), (d), (f) Trailing disk. Solid lines represent drag coefficients and dashed lines represent lift coefficients. The same amplitude logarithmic scale ranging from 0.01 to 500 is used for all the frequency spectra.

As Re increases to 460, the wake becomes weakly chaotic. The frequency spectra of the drag and lift coefficients of both disks illustrate a dominant peak at about $St = 0.145$, and also a second harmonic frequency as shown in Figs. 23(e) and 23(f). But it is noted that the frequency spectra of the drag coefficients of both disks become more complex with broader peaks at $2St$, indicating richer wake dynamics.

For the separation distance of $S/d = 2$, the wake bifurcations become more complex and there are five unsteady states observed. For the Zz -like mode at $Re = 140$, the frequency spectra of the drag coefficient C_d and lift coefficient component C_z for the leading and trailing disk are presented in Figs. 24(a) and 24(b). The frequency spectra of C_d for both disks illustrate dominant peaks at $St = 0.107$, while the spectra of C_z illustrate dominant peaks at $St = 0.107$ and some higher harmonics, indicating the difference from the Zz mode. As shown in Figs. 24(c) and 24(d), for the DHL mode at $Re = 160$, the frequency spectra of lift coefficients of both disks illustrate dominant peaks at $St = 0.107$, while the spectra of the drag coefficients of both disks illustrate dominant peaks at $St = 0.107$ and its harmonics, i.e., $2St$, $3St$, and $4St$, which are related to the periodic shedding of the double-helical structures. For the SW mode at $Re = 170$, similar to the same wake mode when $S/d = 1$ shown in Figs. 23(c) and 23(d), the frequency spectra of lift coefficients of both disks illustrate dominant peaks at $St = 0.107$, while the spectra of drag coefficients of both disks illustrate dominant peaks at $2St$ and even higher harmonics, as shown in Figs. 24(e) and 24(f). However, compared to the spectra in the SW mode for $S/d = 1$, the spectra of the drag coefficients of both disks illustrate broader peaks, indicating richer dynamics at $S/d = 2$. For the RSB-like mode at $Re = 200$, the frequency spectra become a little more complex, as shown in Figs. 24(g) and 24(h). The spectra of the lift coefficients of both leading and trailing disks illustrate sharp peaks at about $St = 0.107$ with a little higher magnitude, while the frequency spectra of drag coefficients of both disks capture dominant peaks at about $2St$. It is noted that the frequency spectra of the drag and lift coefficients of both disks illustrate broader peaks at $2St$ and other higher harmonics with low magnitudes, indicating richer wake dynamics. And one can also note a small bump at a relatively low frequency of about $1/3$ of the vortex shedding frequency in the spectra of the drag coefficients of each disk. For the weakly chaotic state at $Re = 260$, the frequency spectra of drag and lift coefficients of both disks become much more complex as shown in Figs. 24(i) and 24(j). The frequency spectra of lift coefficients of both disks illustrate small peaks at $St = 0.122$ rather than dominant peaks at lower Re , and the spectra of drag coefficients illustrate much broader peaks at $2St$ and other higher harmonics, indicating the weakly chaotic state.

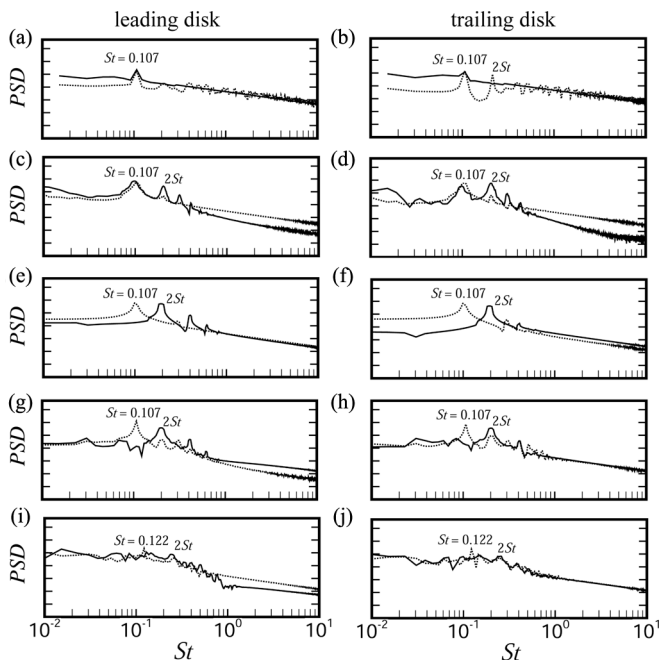


FIG. 24. Frequency spectra of drag and lift coefficients for $S/d = 2$ at (a), (b) $Re = 140$, (c), (d) $Re = 160$, (e), (f) $Re = 170$, (g), (h) $Re = 200$, and (i), (j) $Re = 260$. (a), (c), (e), (g), (i) Leading disk. (b), (d), (f), (h), (j) Trailing disk. Solid lines represent drag coefficients and dashed lines represent lift coefficients. The same amplitude logarithmic scale ranging from 0.01 to 500 is used for all the frequency spectra.

When the separation distance increases to $S/d = 4$, there are four unsteady states captured. For the Zz mode at $Re = 145$, the frequency spectra of the lift coefficients of each disk illustrate a sharp peak at $St = 0.107$, and harmonics with lower magnitudes especially for the trailing disk, as shown in Figs. 25(a) and 25(b). Compared with the Zz mode at $S/d = 1$, the spectra of the drag coefficients illustrate a small peak at $St = 0.107$ but a broader peak with a high magnitude at $2St$, indicating the wake interactions between the two disks. When the wake changes from Zz mode to SW mode at $Re = 160$, the frequency spectra of the force coefficients are similar to the SW mode at $S/d = 1$, i.e., the spectra of lift coefficients of each disk illustrate a dominant peak at $St = 0.114$ while the spectra of drag coefficients of each disk illustrate a broader peak at $2St$ and some higher harmonic frequencies, as shown in Figs. 25(c) and 25(d). For the DHL mode at $Re = 220$, the frequency spectra are similar to those in the SW mode, the spectra of lift coefficients of each disk illustrate a dominant peak at $St = 0.122$, but the peak is much sharper than that in the SW mode, as shown in Figs. 25(e) and 25(f). The spectra of drag coefficients of each disk also capture a broader peak at $2St$. For the weakly chaotic state at $Re = 300$, the frequency spectra also become more complex but a dominant frequency at $St = 0.130$ can be captured, as shown in Figs. 25(g) and 25(h).

For the separation distance of $S/d = 6$, there are also four unsteady states observed. For the RSB-RSB mode at $Re = 150$, the frequency spectra of drag and lift coefficients of both disks illustrate dominant peaks at $St = 0.107$, as shown in Figs. 26(a) and 26(b). Compared with the RSB-like mode for $S/d = 2$, the frequency spectra in the RSB-RSB mode here are more regular. For the SW-SW, DHL, and WC modes, one can note that the frequency spectra of the drag and lift coefficients of both disks are generally very similar to the spectra of those corresponding modes for $S/d = 4$, as shown in Figs. 26(c)–26(h), and even the values of the vortex shedding frequencies are the same. Since the wake interactions decrease when the separation distance increases to $S/d = 6$, the dominant peaks become sharper than those for $S/d = 4$.

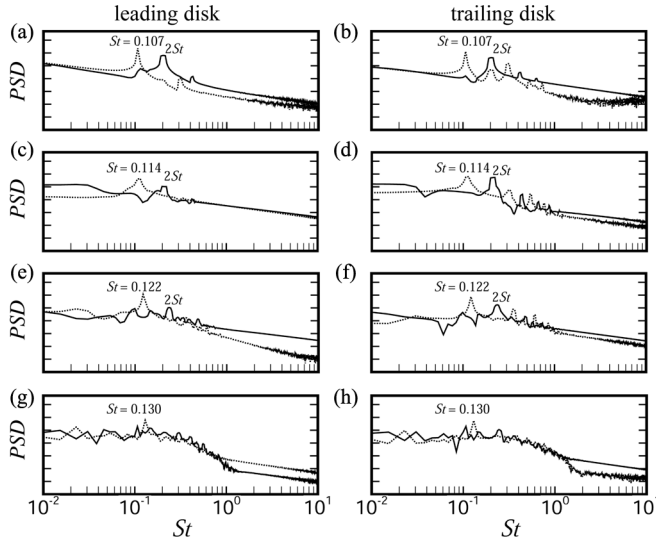


FIG. 25. Frequency spectra of drag and lift coefficients for $S/d = 4$ at (a), (b) $Re = 145$, (c), (d) $Re = 160$, (e), (f) $Re = 220$, and (g), (h) $Re = 300$. (a), (c), (e), (g), (i) Leading disk. (b), (d), (f), (h), (j) Trailing disk. Solid lines represent drag coefficients and dashed lines represent lift coefficients. The same amplitude logarithmic scale ranging from 0.01 to 500 is used for all the frequency spectra.

Figure 27 shows the nondimensional vortex shedding frequency obtained from extensive unsteady states. For $S/d = 1$, the Strouhal number remains constant in this range of Re , and reaches the maximum value at about 0.145. For $S/d = 2$, the Strouhal number remains nearly constant at about 0.107 and then increases to 0.122 in the weakly chaotic state. For $S/d = 4$, the variations

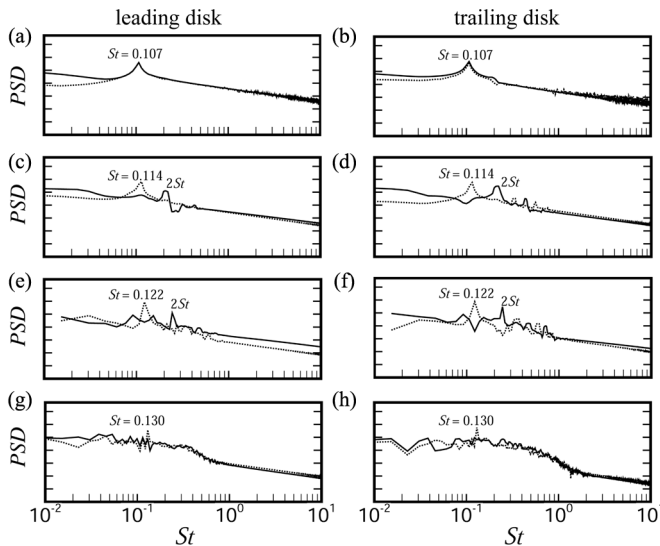


FIG. 26. Frequency spectra of drag and lift coefficients for $S/d = 6$ at (a), (b) $Re = 150$, (c), (d) $Re = 160$, (e), (f) $Re = 220$, and (g), (h) $Re = 300$. (a), (c), (e), (g), (i) Leading disk. (b), (d), (f), (h), (j) Trailing disk. Solid lines represent drag coefficients and dashed lines represent lift coefficients. The same amplitude logarithmic scale ranging from 0.01 to 500 is used for all the frequency spectra.

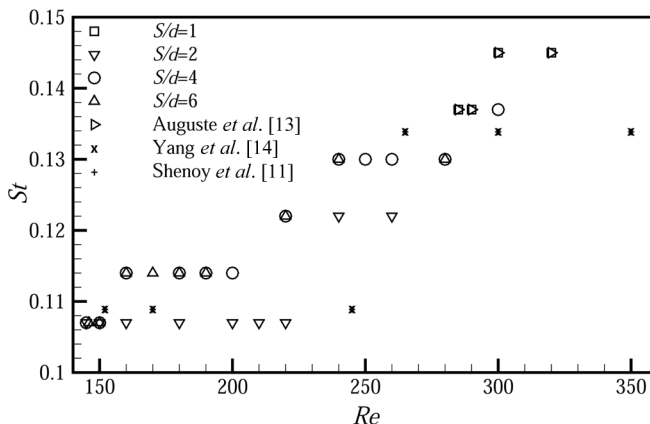


FIG. 27. The nondimensional vortex shedding frequency as a function of Reynolds number at different separation distances. The data for a single disk wake by Auguste *et al.* [13], Shenoy and Kleinstreuer [11], and Yang *et al.* [14] are also included for comparisons

of the Strouhal number are complex and can be divided into five stages. It starts at about 0.107, increases to 0.114 in the SW mode, becomes 0.122 in the DHL mode, and finally increases to 0.130 in the WC mode. As for the case with $S/d = 6$, it is interesting to find that the Strouhal number varies nearly the same as that for $S/d = 4$, confirming weaker interactions when the separation distance increases to 6. For comparisons, the data from a single disk wake are further included in Fig. 27. For the single disk with $\chi = 5$ and 10, the Strouhal number also remains nearly constant at about 0.109, which is slightly higher than the lowest value of the Strouhal number in the tandem disk wake. And then, the Strouhal number increases to 0.134 at higher Re , which compares well with the value of 0.137 obtained in the tandem disk wake for $S/d = 4$ and 6. It is worth noting that the variation of the Strouhal number in a thick disk wake is nearly the same as that in the tandem disk wake with $S/d = 1$. This further indicates that the wake behind two disks closely in tandem is very similar to a single thick disk wake.

F. Flow decomposition

At this point, a deeper analysis of the wake structures using the flow decomposition technique is employed in order to gain further insight into the spatial structures related to each dominant frequency for two wake regimes. Here, a spatial-temporal proper orthogonal decomposition (POD), i.e., the spectral POD (SPOD) [38,39] technique, is used to extract the dominant modes linked to different frequencies. Compared with the traditional (space-only) POD, the SPOD mode describes a structure that evolves coherently both in space and time. For more details on the SPOD, one can refer to Towne *et al.* [38].

For the DH mode at $Re = 160$ and $S/d = 2$, the snapshots of the streamwise vorticity field taken at the cross plane of $x/d = 0.5$ are used to perform the SPOD analysis. Here, 2048 snapshots have been used as the input data. Each snapshot has 73×73 polar grids the maximum radius of which is $R_{\max}/d = 2.45$. Note that the streamwise vorticity snapshots are selected with constant time separation $\Delta t = 0.038 d/U_0$. These temporal parameters could allow us to resolve frequencies between $St_{\min} = 0.0257$ and $St_{\max} = 13.2$.

Figure 28 shows the SPOD energy spectra for the DH mode. It can be found that the SPOD energy spectra for all three modes illustrate dominant peaks at $St = 0.107$ and its harmonics. The dominant frequency $St = 0.107$ is associated with the vortex shedding of the double helical vortex structures, the value of which is equal to that captured in the frequency spectra of drag or lift coefficients shown in Figs. 24(c) and 24(d). It is noted that harmonics have also been observed in the frequency spectra

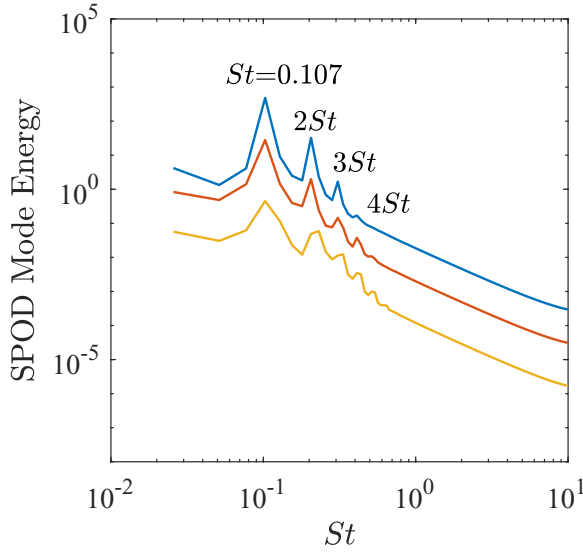


FIG. 28. SPOD energy spectra for the DH mode at $Re = 160$ and $S/d = 2$. The blue, orange, and yellow lines represent the modes 1, 2, and 3, respectively.

of the drag or lift coefficients. The SPOD mode 1 as indicated by the blue line in Fig. 28 accounts for 97.30% of the total energy, while the SPOD modes 2 and 3 indicated by the orange and yellow lines only capture 2.57 and 0.13% of the total energy, respectively. It indicates the SPOD mode 1 dominates the wake structures. Furthermore, the SPOD mode 1 at $St = 0.107$ captures the highest energy, which is about 73.22% of the total energy. It indicates that the SPOD mode 1 at $St = 0.107$ represents the dominant wake structures. It is noted that the SPOD modes 1 at $St = 0.107$ and its harmonics $2St$ and $3St$ account for 91.87% of the total energy. And these three SPOD eigenfunctions will then be inspected to understand the wake structures in the DH wake regime.

Figure 29 presents the spatial-temporal SPOD modes (eigenfunctions) 1 at $St = 0.107$ and its harmonics $2St$ and $3St$. An instantaneous snapshot is also given for comparison, as shown in Fig. 29(a). Due to the double-helical structures observed shown in Fig. 11(a), the streamwise vorticity snapshot illustrates a similar yin-yang shape. The most energetic mode, i.e., SPOD mode 1 at $St = 0.107$, corresponds to a m_1 symmetry and resembles the yin-yang mode, as shown in Fig. 29(b). Since this SPOD mode accounts for 73.22% of the total energy, it resembles the instantaneous snapshot. The second energetic mode, i.e., SPOD mode 1 at $2St = 0.214$, illustrates a quadrupole of vorticity compatible with a $m = 2$ symmetry, as shown in Fig. 29(c). Figure 29(d) shows the SPOD mode 1 at $3St = 0.321$, illustrating a sextupole of vorticity. These three SPOD modes mainly govern the flow dynamics in the DH wake regime. We note that the double-helical wake structure has been previously observed in the wake behind a rotating sphere (e.g., Lorite-Diez and Jimenez-Gonzalez [40]). In their work, the same yin-yang mode has also been observed corresponding to a m_1 symmetry using the HODMD (High order dynamic mode decomposition) decomposition technique. Moreover, the quadrupole of vorticity with a $m = 2$ symmetry has also been captured (see Fig. 7 in [40]).

For the DHL mode at $Re = 220$ and $S/d = 4$, the appearance of double-hairpin loops in the downstream wake behind the trailing disk is the main flow feature for this wake regime. And thus the snapshots of the streamwise vorticity field taken at the cross plane of $x/d = 4.5$ are used to perform the SPOD analysis. Here, the number of snapshots and the grid resolution for each snapshot are all the same as the DH case. The streamwise vorticity snapshots are equispaced in time with

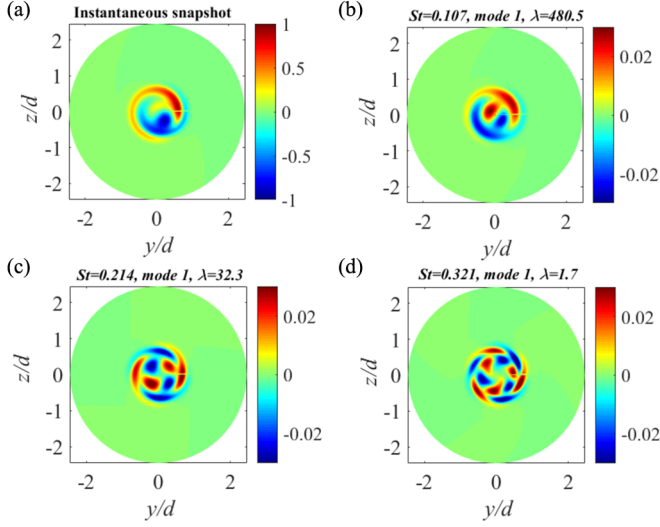


FIG. 29. (a) The instantaneous snapshot of the contours of streamwise vorticity, and the dominant SPOD modes at (b) $St = 0.107$, (c) $2St = 0.214$, and (d) $3St = 0.321$, for $Re = 160$ and $S/d = 2$.

$\Delta t = 0.032 d/U_0$. These temporal parameters allow resolving frequencies between $St_{\min} = 0.0305$ and $St_{\max} = 15.6$.

Figure 30 shows the SPOD energy spectra for the DHL mode. Different from the spectra in the DH mode, only SPOD energy spectra for mode 1 illustrate dominant peaks at $St = 0.122$ and its harmonics. The dominant frequency $St = 0.122$ is associated with the vortex shedding of the hairpin vortex structures, the value of which is equal to that captured in the frequency spectra of drag or lift coefficients shown in Figs. 25(e) and 25(f). It is noted that many harmonics have also been observed in the frequency spectra of the drag or lift coefficients. SPOD mode 1 as indicated by the blue line in Fig. 30 accounts for 99.86% of the total energy. It indicates that the SPOD mode 1 predominates

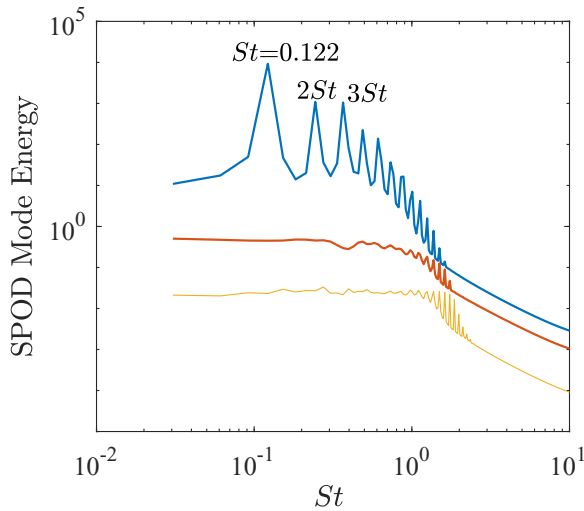


FIG. 30. SPOD energy spectra for the DHL mode at $Re = 220$ and $S/d = 4$. The blue, orange, and yellow lines represent the modes 1, 2, and 3, respectively.

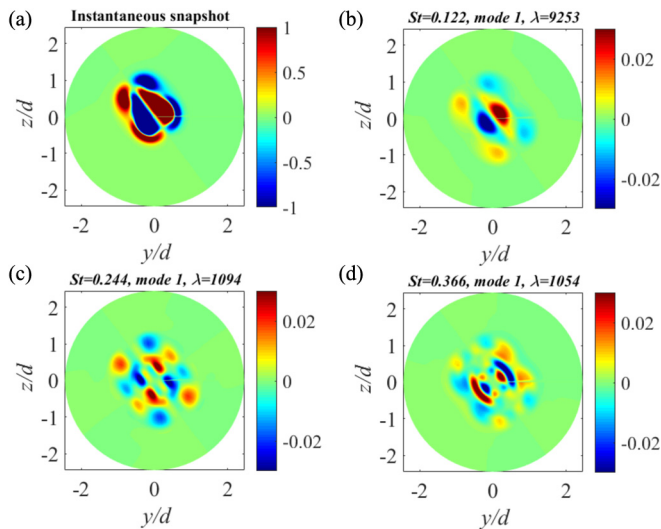


FIG. 31. (a) The instantaneous snapshot of the contours of streamwise vorticity, and the dominant SPOD modes at (b) $St = 0.122$, (c) $2St = 0.244$, and (d) $3St = 0.366$, for $Re = 220$ and $S/d = 4$.

the wake dynamics. Similarly, the SPOD mode 1 at $St = 0.122$ captures the highest energy, which is about 74.66% of the total energy. It indicates that the SPOD mode 1 at $St = 0.122$ represents the dominant wake structures. It is also noted that the SPOD modes 1 at $St = 0.122$ and its harmonics $2St$ and $3St$ account for 92.00% of the total energy.

Figure 31 shows the spatial-temporal SPOD modes (eigenfunctions) 1 at $St = 0.122$ and its harmonics $2St$ and $3St$. An instantaneous snapshot is also given for comparison, as shown in Fig. 31(a). Due to the double-helical structures observed shown in Fig. 17(a), the streamwise vorticity snapshot illustrates planar symmetry with three pairs of vortices. The most energetic mode, i.e., SPOD mode 1 at $St = 0.122$, also illustrates the planar symmetry and resembles the instantaneous snapshot. The second energetic mode, i.e., SPOD mode 1 at $2St = 0.244$, also illustrates a quadrupole of vorticity compatible with a $m = 2$ symmetry, as shown in Fig. 31(c). Figure 31(d) shows the SPOD mode 1 at $3St = 0.366$, illustrating a more complex structure resulting from the higher harmonic frequency.

IV. COMPARISON BETWEEN THE WAKES OF TANDEM DISKS AND A SINGLE DISK

As demonstrated above, the wake regime behind two circular disks in tandem arrangement is strongly dependent on the separation distance between them as well as the Reynolds number. In the present considered parametric space, seven main wake bifurcations are observed, namely, SS, periodic state with planar symmetry but nonzero mean lift or Zz mode, periodic state with planar symmetry and zero-mean lift or SW mode, periodic state with RSB, periodic state with DH structures shedding, periodic state with DHL shedding, and WC state. In the steady state, three subregimes have been further identified, i.e., SS-AS mode, SS mode, and SS-SS mode. For the RSB mode, three subregimes have been identified, i.e., RSB-like mode, RSB mode, and RSB-RSB mode. Similarly, two subregimes have been identified for the SW mode, i.e., SW mode and SW-SW mode. Figure 32 presents the wake regime map in the considered $(Re, S/d)$ space. To compare with the wake transition scenarios behind a single disk, the corresponding wake regimes in the single disk wake from our previous work [14] are also included.

It can be found that the first bifurcation leading to the SS mode is always delayed in tandem configuration, especially for the case of $S/d = 1$. As for the second bifurcation leading to the unsteady state, the differences lie in the wake mode for different tandem configurations. When

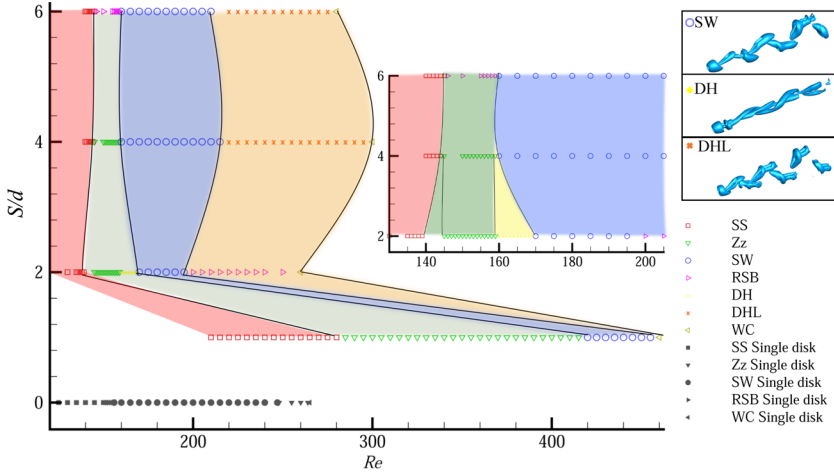


FIG. 32. Wake regimes behind tandem disks in the $(Re, S/d)$ map. For the sake of comparison, the numerical results for a single disk wake from Yang *et al.* [14] (gray filled symbols) are also included. The different wake regimes are denoted as \square SS (steady state), ∇ Zz (Zig-zig mode), \circ SW (standing wave mode), \triangleright RSB (periodic state with reflectional symmetry breaking), $+$ DH (periodic state with double-helical structures shedding), \times DHL (periodic state with double-hairpin-loop shedding), and \triangleleft WC (weakly chaotic state). Three typical unsteady regular wake structures depicted by the isosurface of the Q criterion are also illustrated.

$S/d = 1, 2,$ and 4 , the second bifurcation leads to the Zz wake mode, while it leads to the RSB mode in the case of $S/d = 6$ and the single disk wake. Through careful comparisons with the bifurcation scenarios in the corresponding single disk wake, one can find that the bifurcation scenarios for $S/d = 6$ are very similar to those of a single disk wake, except a DHL wake mode is observed in the tandem configuration. Among all the cases considered, the bifurcation scenarios for $S/d = 2$ are the most complex and quite different from those in a single disk wake. This indicates that the interaction between two disks in tandem arrangement is much stronger when the trailing disk is located at the near end of the recirculation region of the leading one. Also, it is noted that the RSB mode is only observed in the cases of $S/d = 2$ and 6 , which is associated with the very limited conditions for the occurrence of the RSB wake mode.

Furthermore, the ratios of critical Reynolds numbers in the wake of tandem disks to those in a single disk wake for the first two bifurcations are plotted in Fig. 33. Both the wakes of tandem

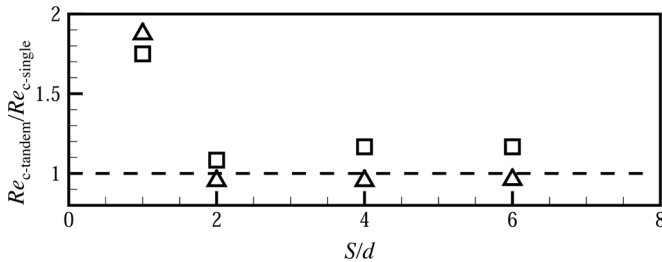


FIG. 33. The ratios of critical Reynolds numbers for the first two bifurcations in the wake of tandem disks to those in a single disk wake. \square represents the ratio of the first critical Reynolds number leading to the SS wake mode, while \triangle represents the ratio of the second critical Reynolds number leading to an unsteady state with vortex periodically shedding. A horizontal dashed line represents the value of 1.

disks and a single disk are steady and axisymmetric at low enough Reynolds numbers. Beyond a first critical Reynolds number, Re_{c1} , the axial symmetry is broken and the wake changes to a steady state with planar symmetry (SS mode). Beyond a second critical Reynolds number Re_{c2} the wake becomes unsteady with vortex shedding, although this bifurcation could lead to different wake modes. As shown in Fig. 33, it also clearly shows that the critical Reynolds numbers of both the first two bifurcations are much delayed in the wake behind tandem disks with the separation distance $S/d = 1$. As the separation distance increases from 1 to 2, the ratio decreases rapidly close to 1. For the cases of $S/d = 4$ and 6, the ratio varies little. It is worth noting that the critical Reynolds number for the first bifurcation is always higher than that in a single disk wake and will vary slowly towards 1 when the separation distance is long enough, while the critical Reynolds number for the second bifurcation is a little lower than that in a single disk wake except for the case of $S/d = 1$, indicating the wake will become unsteady earlier in the wakes behind tandem disks except for the situation of a very short separation distance between two disks.

V. CONCLUSION

The wake bifurcation scenarios behind two circular disks in the tandem arrangement are carefully explored through a series of well-designed numerical simulations. It is found that the wake bifurcations have a strong dependence on the separation distance between the two disks as well as the Reynolds number. In the present (Re , S/d) space, seven main wake regimes are identified based on the flow topography and characteristics of the force coefficients: SS, periodic state with planar symmetry but nonzero mean lift or Zz mode, periodic state with planar symmetry and zero-mean lift or SW mode, periodic state with RSB, periodic state with DH structures shedding, periodic state with DHL shedding, and WC state. Compared with the single disk wake, the first bifurcation leading to the SS mode is always delayed especially in the case of $S/d = 1$. As for the second bifurcation leading to an unsteady state, different wake bifurcations are observed for different tandem configurations. When $S/d = 1, 2$, and 4, the second bifurcation leads to the Zz wake mode, while it leads to the RSB mode for the case of $S/d = 6$ and the single disk wake. Through careful comparisons with the bifurcation scenarios in the corresponding single disk wake, it is found that the bifurcation scenarios for $S/d = 1$ are similar to those of a thick disk, suggesting that the circular disks, when placed very closely in tandem, are similar to the situation of increasing the thickness of a single disk. The bifurcation scenarios for $S/d = 2$ are the most complex and quite different from those in a single disk wake, indicating that the stronger interactions between two disks in tandem arrangement appear when the trailing disk is located close to the near end of the recirculation region of the leading one. The bifurcation scenarios for $S/d = 6$ are very similar to those of the single corresponding disk wake, except a DHL wake mode is observed in tandem due to the interactions between the vortex loops shed, respectively, from the leading and trailing disk. In addition, the RSB mode is only observed in the cases of $S/d = 2$ and 6, which is associated with the very limited conditions for the occurrence of the RSB wake mode.

ACKNOWLEDGMENTS

This work has been partially supported by the National Natural Science Foundation of China (Grants No. 11947012 and No. 51806001), Anhui Provincial Natural Science Foundation (Grant No. 1908085MA08), and Fundamental Research Funds for the Central Universities (Grant No. JZ2021HG7B0122). The authors would like to thank the Supercomputing Center of University of Science and Technology of China for providing computer resources.

[1] P. Ern, F. Risso, D. Fabre, and J. Magnaudet, Wake-induced oscillatory paths of bodies freely rising or falling in fluids, *Annu. Rev. Fluid Mech.* **44**, 97 (2012).

- [2] R. Natarajan and A. Acrivos, The instability of the steady flow past spheres and disks, *J. Fluid Mech.* **254**, 323 (1993).
- [3] B. Ghidersa and J. Dusek, Breaking of axisymmetry and onset of unsteadiness in the wake of a sphere, *J. Fluid Mech.* **423**, 33 (2000).
- [4] T. A. Johnson and V. C. Patel, Flow past a sphere up to a Reynolds number of 300, *J. Fluid Mech.* **378**, 19 (1999).
- [5] A. G. Tomboulides and S. A. Orszag, Numerical investigation of transitional and weak turbulent flow past a sphere, *J. Fluid Mech.* **416**, 45 (2000).
- [6] M. C. Thompson, T. Leweke, and M. Provansal, Kinematics and dynamics of sphere wake transition, *J. Fluids Struct.* **15**, 575 (2001).
- [7] D. Ormieres and M. Provansal, Transition to Turbulence in the Wake of a Sphere, *Phys. Rev. Lett.* **83**, 80 (1999).
- [8] S. S. Tiwari, S. Bale, A. W. Patwardhan, K. Nandakumar, and J. B. Joshi, Insights into the physics of dominating frequency modes for flow past a stationary sphere: Direct numerical simulations, *Phys. Fluids* **31**, 045108 (2019).
- [9] D. Fabre, F. Auguste, and J. Magnaudet, Bifurcations and symmetry breaking in the wake of axisymmetric bodies, *Phys. Fluids* **20**, 051702 (2008).
- [10] H. Sakamoto and H. Haniu, A study on vortex shedding from spheres in a uniform flow, *J. Fluids Eng.* **112**, 386 (1990).
- [11] A. R. Shenoy and C. Kleinstreuer, Flow over a thin circular disk at low to moderate reynolds numbers, *J. Fluid Mech.* **605**, 253 (2008).
- [12] P. C. Fernandes, F. Risso, P. Ern, and J. Magnaudet, Oscillatory motion and wake instability of freely rising axisymmetric bodies, *J. Fluid Mech.* **573**, 479 (2007).
- [13] F. Auguste, D. Fabre, and J. Magnaudet, Bifurcations in the wake of a thick circular disk, *Theor. Comput. Fluid Dyn.* **24**, 305 (2010).
- [14] J. Yang, M. Liu, G. Wu, W. Zhong, and X. Zhang, Numerical study on instabilities behind a circular disk in a uniform flow, *Int. J. Heat Fluid Flow* **50**, 359 (2014).
- [15] M. Chrust, G. Bouchet, and J. Dusek, Parametric study of the transition in the wake of oblate spheroids and flat cylinders, *J. Fluid Mech.* **665**, 199 (2010).
- [16] S. Gao, L. Tao, X. Tian, and J. Yang, Flow around an inclined circular disk, *J. Fluid Mech.* **851**, 687 (2018).
- [17] V. L. Okulov, I. V. Litvinov, I. V. Naumov, and R. Mikkelsen, Self-similarity of far wake behind tandem of two disks, *J. Eng. Thermophys.* **26**, 154 (2017).
- [18] C. Zhu, S. C. Liang, and L. S. Fan, Particle wake effects on the drag force of an interactive particle, *Int. J. Multiphase Flow* **20**, 117 (1994).
- [19] S. C. Liang, T. Hong, and L. S. Fan, Effects of particle arrangements on the drag force of a particle in the intermediate flow regime, *Int. J. Multiphase Flow* **22**, 285 (1996).
- [20] R. Chen and Y. Lu, The flow characteristics of an interactive particle at low reynolds numbers, *Int. J. Multiphase Flow* **25**, 1645 (1999).
- [21] Y. Tsuji, Y. Morikawa, and K. Terashima, Fluid-dynamic interaction between two spheres, *Int. J. Multiphase Flow* **8**, 71 (1982).
- [22] J. F. Zou, A. L. Ren, and J. Deng, Study on flow past two spheres in tandem arrangement using a local mesh refinement virtual boundary method, *Int. J. Numer. Methods Fluids* **49**, 465 (2005).
- [23] L. Prahla, A. Jadoon, and J. Revstedt, Interaction between two spheres placed in tandem arrangement in steady and pulsating flow, *Int. J. Multiphase Flow* **35**, 963 (2009).
- [24] D. H. Yoon and K. S. Yang, Characterization of flow pattern past two spheres in proximity, *Phys. Fluids* **21**, 073603 (2009).
- [25] R. F. Huang, L. M. Duc, and C. M. Hsu, Effects of swirling strength on flow characteristics of swirling double-concentric jets with a dual-disk flow controller, *Exp. Therm. Fluid Sci.* **68**, 612 (2015).
- [26] R. F. Huang and S. C. Yen, Axisymmetric swirling vortical wakes modulated by a control disc, *AIAA J.* **41**, 888 (2003).

- [27] N. Brosse and P. Ern, Paths of stable configurations resulting from the interaction of two disks falling in tandem, *J. Fluids Struct.* **27**, 817 (2011).
- [28] N. Brosse and P. Ern, Interaction of two axisymmetric bodies falling in tandem at moderate Reynolds numbers, *J. Fluid Mech.* **757**, 208 (2014).
- [29] T. Morel and M. Bohn, Flow over two circular disks in tandem, *J. Fluids Eng.* **102**, 104 (1980).
- [30] M. Liu, C. Xie, J. Yang, X. Zhu, and M. Yao, Numerical study on the flow over two circular disks in tandem arrangement, *Phys. Fluids* **31**, 034102 (2019).
- [31] M. Germano, U. Piomelli, P. Moin, and W. H. Cabot, A dynamic subgrid-scale eddy viscosity model, *Phys. Fluids* **3**, 1760 (1991).
- [32] M. Breuer, J. Bernsdorf, T. Zeiser, and F. Durst, Accurate computations of the laminar flow past a square cylinder based on two different methods: Lattice-Boltzmann and finite-volume, *Int. J. Heat Fluid Flow* **21**, 186 (2000).
- [33] J. Yang, M. Liu, G. Wu, W. Zhong, and X. Zhang, Numerical study on coherent structure behind a circular disk, *J. Fluids Struct.* **51**, 172 (2014).
- [34] J. Yang, M. Liu, G. Wu, Q. Liu, and X. Zhang, Low-frequency characteristics in the wake of a circular disk, *Phys. Fluids* **27**, 064101 (2015).
- [35] Y. Morinishi, T. S. Lund, O. V. Vasilyev, and P. Moin, Fully conservative higher order finite difference schemes for incompressible flow, *J. Comput. Phys.* **143**, 90 (1998).
- [36] J. C. R. Hunt, A. A. Wray, and P. Moin, Eddies, streams, and convergence zones in turbulent flows, in *Proceedings of the Summer Program in Center for Turbulence Research*, 1988 (unpublished), p. 193.
- [37] J. Yang, M. Liu, C. Wang, X. Zhu, and A. Zhang, Numerical study on uniform-shear flow over a circular disk at low Reynolds numbers, *Phys. Fluids* **30**, 083605 (2018).
- [38] A. Towne, O. T. Schmidt, and C. Tim, Spectral proper orthogonal decomposition and its relationship to dynamic mode decomposition and resolvent analysis, *J. Fluid Mech.* **847**, 821 (2018).
- [39] A. Nekkanti and O. T. Schmidt, Frequency-time analysis, low-rank reconstruction and denoising of turbulent flows using SPOD, *J. Fluid Mech.* **926**, A26 (2021).
- [40] M. Lorite-Díez and J. I. Jimenez-Gonzalez, Description of the transitional wake behind a strongly streamwise rotating sphere, *J. Fluid Mech.* **896**, A18 (2020).

Correction: The last column of Table I contained a typographical error and has been fixed.